

Anonymous Referee #1

Received and published: 9 September 2019

We wish to thank the referee for his/her helpful comments. The full reviews are copied hereafter and our responses are inserted. The comments of the reviewer are in normal black and our answers in bold.

This paper describes a Bayesian inverse modeling system for reactive compounds, PYVAR-CHIMERE. It also provides an illustration of what this system can do with two one-day inversions of emissions over Europe. The paper is generally well written, and the topic of the paper is relevant for this journal. Although the results indicate that the system has potential, there are several major issues which should be dealt with before this work can be published in GMD.

1) poor quality of the figures and equations. On the screen, it is more or less acceptable (with the zoom in feature of my pdf viewer), but upon printing, many figures (especially Figs. 1-4 and Figs. 6a and 8a) and equations are impossible to read.

We apologize, the poor quality in particular of the equations was due to conversion from OpenOffice to pdf. The resolution of the equations and of the figures has been improved.

Figure 3 is really a Table and should be inserted as such.

We agree, Figure 3 is now the Table 1.

Some mathematical symbols (e.g. gradient on line 158, multiplication on line 167) are inappropriate.

These symbols have been corrected.

2) Section 3.2 is 'Development of the adjoint of CHIMERE'. But the adjoint of CHIMERE was developed a long time ago (publications by L. Menut, I. Pison). What are the specific developments realized for this study, besides the minor changes to CHIMERE mentioned in the text?

Indeed, the adjoint of CHIMERE was developed a long time ago. We first have changed the title section into "Development and parallelization of the adjoint and tangent-linear codes of CHIMERE".

We added sentences in Section 3.1: "PYVAR has been adapted to CHIMERE with an adjoint code without chemistry a first time by Broquet et al. [2011]. In order to couple PYVAR to the new state-of-the-art version of CHIMERE (see Section 3.2), to include chemistry, and to increase its modularity, flexibility and clarity, the new system described here has been developed. It includes elements of the inversion system (coded in Fortran90) of [Pison et al., 2007]."

Efforts have indeed been made for the parallelization of the code. This is now explained in the text in Section 3.2: "Then, it has been parallelized at LSCE and LISA. This work required a redesigning of the whole code, associated with a full testing scheme. Furthermore, the tangent-linear (TL) code has been developed and validated at LSCE. Changes have been implemented in the forward CHIMERE code embedded in PYVAR-CHIMERE to match requirements of the studies lead with PYVAR-CHIMERE. These changes have been implemented in both the adjoint and the TL codes. Compared to the CHIMERE 2013 version [Menut et al., 2013], the most important of these changes are:

- For the geometry, the possibility of polar domains and the use of the coordinates of the corners of the cells instead of only the centers**
- For the transport, the non-uniform Van Leer transport scheme on the horizontal,**

•For chemistry, various switches have been added to avoid going into the chemistry, deposition and wet deposition routines when no species requires them (e.g. no chemistry for methane at a regional scale).”

3) the results of inverse modeling studies are very dependent on the inversion setup, in particular the definition of the control vector and the construction of the covariance matrices R and especially B. What is the strategy in this regard? I understand that the main purpose of the paper is less to present specific inversion studies than to describe the general modeling framework. But the very simplistic choices made for the two one-day inversions suggest an absence of any strategy. The chemical lifetimes of the target species, the duration of the experiments, the initial and boundary conditions, and the assumed a priori uncertainties should all play a role in the inverse setup definition.

Indeed, we agree, the main purpose of a GMD paper is less to present specific inversion studies than to describe the general modeling framework. Nevertheless, we added information to explain our choices of illustrations in the introduction of Section 4: "We have chosen to present illustration of CO inversion over a 7-day window, the first week of March 2015. Considering the short lifetime of NO_x of a few hours [Valin et al., 2013; Liu et al., 2016], we have chosen to present illustration of NO_x inversion over a 1-day window, the 19th February 2015. These particular periods have been chosen as they present a representative number of super-observations during winter, and as the emissions are high during that period."

We also have added a new "Section 4.2.2. Covariance matrices B and R" to better describe the covariance matrices B and R.

4) the two illustrations of PYVAR-CHIMERE capabilities are unconvincing. Yes, the system finds a minimum to the cost function, and the a posteriori simulation matches the observations quite well; but no, the a posteriori emissions are not shown to be closer to reality. With its long lifetime, CO is largely determined by the initial and lateral boundary conditions, which are part of the control state vector being optimized. The paper does not provide information on the a priori uncertainties for these parameters. A discussion is needed, and possibly sensitivity simulations.

We now provide more information about the initial, lateral and top boundary conditions in the new "Section 4.1.2. CHIMERE set-up": "Different climatological values from the LMDZ-INCA global model [Szopa et al., 2008] or from a MACC reanalysis are used to prescribe concentrations at the lateral and top boundaries and the initial atmospheric composition in the domain."

Information on the prior uncertainties was given in the former Figure 3, now replaced by Table 1. We also added sensitivity tests in Section 4.1.3: "With its lifetime of about two months, CO could be strongly driven by the initial and lateral boundary conditions prescribed in the CTM. In fact, as seen in Figure 4b, initial and boundary conditions provide a relatively flat background and the patterns which appear clearly over the background are linked to surface emissions (Figure 4a). To characterize the uncertainties in the concentration fields due to the initial and lateral boundary conditions, we performed a sensitivity test by using either climatological values from LMDZ-INCA or a MACC reanalysis: the results were not significantly different, with relative differences in concentrations of less than 15% over continental land (Figure 5c)."

We also added text in the new "Section 4.2.2. Covariance matrices B and R": "Based on the sensitivity test in Figure 5, the errors assigned to the CO lateral and top boundary conditions and to their initial conditions are set at 15%. As these relative errors are significantly lower than those for the emissions and as variations in the CO surface concentrations are mainly

driven by emissions (Figure 4), we assume a small relative influence of the correction of initial and boundary conditions on our results. "

Note that, although the a priori simulation overestimates CO over Central Europe (south of Poland), the inversion increases the emissions there by about a factor of 2! Over Germany, the emissions are almost doubled in the Southern part, but are unchanged elsewhere. How can this be justified?

Figure 6 has been updated. The emissions are increased over Central and Eastern Europe, except in the south of Poland.

Even for NO_x, in spite of their shorter lifetime, the initial and boundary conditions play probably a very important role.

We also checked the impact of initial and boundary conditions on NO₂ tropospheric columns. Due to its short lifetime, the impact is even smaller than for CO. We chose not to show this sensitivity test in the paper.

The discussion of the results for NO_x (lines 373-376) is impossible to understand. It says that the optimization of NO_x fluxes has only a small impact on the model biases. This is not true. Comparison of Fig. 7c and 7d show that the optimization works very well!

We do not agree, as Fig 7c and Fig 7d were not comparable (they did not have the same legend). Nevertheless, we agree, it could have been confusing. We now present the impact of the optimization of the NO_x fluxes differently, in Figure 7.

The authors claim that PYVAR optimizes only the NO₂ fluxes, not those of NO. I don't believe this, it doesn't make sense. Please check this. In any case, clarifications and possibly a sensitivity analysis are in order.

As both the reviewers have been disturbed by the illustration with only NO₂ fluxes, we now present inversion for NO_x emissions.

Other comments:

- throughout the text, replace "NO₂ emissions" by "NO_x emissions" (if indeed, as should be the case, NO_x emissions are optimized, not just NO₂)

See comments above. "NO₂ emissions" have indeed been replaced by "NO_x" emissions throughout the text.

- lines 107-110: please refer also to GEOS-Chem adjoint papers (Henze, Kopacz, Cao et al.)

A reference to Henze et al. 2007 has been added. A reference to the adjoint-based four-dimensional variational (4D-Var) assimilation system, WRF-CO₂ 4D-Var, has also been added.

- l. 149 what is meant by "the control of emissions"?

We have rephrased: "By definition, the observation errors combine errors in both the data and the observation operator, in particular measurement errors and errors in the conversion of satellite measurement into concentration data, errors from the CTM, representativity errors due to the comparison between point measurements and gridded models or due to the representation of the fluxes as gridded maps at a given spatial resolution, and aggregation errors associated with the optimization of emissions at a given spatial and/or temporal resolution (as specified in the control vector) that is different from (usually coarser than) that of the CTM [Wang et al., 2017]."

-l. 168-169 What are the thresholds for the ratio between final and initial gradient norm, and for the number of iterations?

This information was already given in Section 4. It is now in the introduction of Section 4: "For practical purposes, we recommend to reduce the norm of the gradient of J by 90%. We no longer give information about the number of iterations as it depends on each configuration system. These information are now given in Section 4.2.3 for CO: " Ten iterations are needed to reduce the norm of the gradient of J by 90% with the minimization algorithm M1QN3" and in Section 4.2.4 for NO_x: "Six iterations are needed to reduce the norm of the gradient of J by 85% with the minimization algorithm M1QN3".

-Figure 1. In the orange box on the right, the order of operators should go backwards, shouldn't they?

Indeed, the adjoint go backwards but these operations are made simultaneously in CHIMERE.

- l. 195 leads (instead of lead)

It has been changed.

-Figure 3. Explain the meaning of the "correction type" and of the three numbers in column "B variance coefficients".

The correction type describes the way the emissions are corrected by the inversion. We have added the following descriptions in "Section 3.3. Definition of the control vector": "Several types of corrections can be applied, they are defined in the code as "add", "mult" or "scale". Both the corrections "add" and "mult" are applied to gridded control variables. For correction type "add" the control variables are increments added to the corresponding components of the model inputs. For correction type "mult", the control variables are scaling factors multiplying the corresponding components of the model inputs. The difference between the two options "add" and "mult" plays a role when inverting fluxes which can switch from positive to negative values (like CO₂ natural fluxes). For type "scale", the corrections consist in applying scaling factors to activity maps and/or masks for regions (which is similar to the control of budgets for different regions, types of activities, and/or processes in inversions where the control vector is not gridded [Wang et al., 2018]) and adding the obtained values to the corresponding components of the model inputs."

The three numbers in column "B variance coefficients" are standard deviation coefficient. We have added information: "The variances are specified by the user through standard deviation coefficient (Table 1), which can be a fixed value ("fx") or a percentage ("pc") to define the diagonal standard deviation matrix Σ ."

- Figure 4. The legends mentions text in blue and in grey. I don't see that on the figure. Is this figure useful?

The sentence mentioning text in blue and in grey has been removed.

- l. 298 What is the resolution of ECMWF data? Are those data interpolated to the model grid?

The spatial resolution of the ECMWF data is 0.25°x0.25°. They have been interpolated to the model grid.

-l. 300 Derognat et al. 2003 does not present a chemical mechanism, but refers to earlier papers.

The reference to Derognat has been removed. We now refer to Lattuati, 1997 and to the latest CHIMERE documentation. The text is now:"The chemical scheme used in PYVAR-CHIMERE is MELCHIOR-2, with more than 100 reactions [Lattuati, 1997; CHIMERE 2017], including 24 for inorganic chemistry".

-What are the a priori lateral boundary conditions?

The prior lateral and top boundary conditions are climatological values from the LMDZ-INCA global model [Szopa et al., 2008]. It was indicated in Section 4.1.1. We now describe them in "Section 4.1.2 CHIMERE set-up" and we also made a sensitivity test with a MACC reanalysis in "Section 4.1.3. Sensitivity to emissions and to initial and boundary conditions".

- on l. 303 and legend of Fig. 8, the information required to run the inversion are said to be listed in Table 1. This is not correct.

We agree, this is now true (Figure 3 is now called Table 1).

- l. 304 Are only anthropogenic emissions optimized? Or the total of all emissions?

Only the anthropogenic emissions are optimized here. This is now written in the introduction of Section 4: "The potential of the PYVAR-CHIMERE system to invert emissions of reactive species is illustrated with the inversion of CO and NO_x anthropogenic emissions in Europe respectively based on MOPITT CO data and OMI NO₂ data".

This is also now written in the description of the control vectors in Section 4.2.1.

-l. 306-307 The 3D initial conditions at the model resolution are said to represent 8585 components of the control vector. But what about the vertical dependence?

The vertical dependence is indeed taken into account. The number of components in the control vector has been corrected.

-l. 311-314 What are the non-anthropogenic emissions used in the model?

The biogenic emissions, that we assume negligible in winter, are not used in our illustration. In addition, we should have described that PYVAR-CHIMERE only infers anthropogenic emissions at this stage. This is now added in Section 3.2 : "It should also be noted that PYVAR-CHIMERE only infer anthropogenic emissions at this stage. The optimization of biogenic emissions, which are linearly interpolated at the sub-hourly scale in CHIMERE, is currently under development."

-Please provide a webpage and reference for EMEP emissions. Aren't there any publication or webpage for the TNO emissions?

We now provide two references for the EMEP emissions (a publication and a webpage). We also provide a reference for the TNO-GHGco used in this paper (submitted in December 2019 and published in February 2020). The text is now: "The prior anthropogenic emissions for CO and NO_x emissions come from the TNO-GHGco-v1 inventory [Super et al., 2020], the last update of the TNO-MACCII inventory [Kuenen et al., 2014]. The prior anthropogenic emissions for VOCs come from the EMEP inventory [Vestreng et al., 2005; EMEP/CEIP website]."

-l. 328 Why the median?

The median is chosen here to take proper account of the AKs (we can not take the mean of the AKs).

-l. 341 With errors of 100% on the emissions, how can negative a posteriori emissions be avoided? How is this dealt with?

We now answered to this remark in "Section 4.2.2. Covariance matrices B and R": "With such a set-up, in theory, we could obtained negative posterior emissions since the inversion system does not impose a constraint of positivity in the results. Nevertheless, even 100% of uncertainty lead to a prior distribution mostly (>80%) on the positive side. The assimilation of data showing an increase above the background (at the edges of the domain; not shown)

further drive the inversion towards positive emissions for both CO and NO_x inversions. In practice, our inversion does not lead to negative posterior emissions (Figure 7b). Spatial and temporal correlations in B would further limit the probability to get negative emissions locally by smoothing the posterior emissions at a spatial scale at which the “aggregated” prior uncertainty is smaller than 100%. However, a positivity constraint should be implemented in future versions of the system."

-Section 4.2 The Figure 5 shows both underestimations and overestimations by the apriori simulation. This is not well reflected in the discussion.

Indeed, this is now reflected in the discussion in Section 4.2.3.

-Figure 7c and 7d should show absolute differences.

We no longer present these figures.

-A better color scale should be possible for Fig. 7a and 7c

Indeed, it has been done in Figure 8 and in Figure 10.

We wish to thank the referee for his/her helpful comments. The full reviews are copied hereafter and our responses are inserted. The comments of the reviewer are in normal black and our answers in bold.

The paper describes the variational data assimilation version of the CHIMERE, PYVAR-CHIMERE, which is capable of inversions of reactive gases. As a demonstration to the newly developed code, the inversion of CO and NO₂ is shown for two different days in late winter/early spring 2015. The paper's topic is of good relevance for GMD and contributes to a documented open source regional data assimilation system for reactive chemistry. Although the paper is generally well written, major changes are requested before publishing the manuscript in GMD.

These major changes are:

- The quality of figures and formulas is unacceptable. Arrows should be larger/thicker (Fig. 1 and 2), annotations in Figs. 5, 6, 7, and 8 are too small, separation of subplots and 7 should be clearer.

The quality of all the figures has been improved.

- The description of the inversion is unsatisfactory. The cost function and its gradient should explicitly show the model operator M , which is currently included in the state vector x .

We do not agree with this statement, the model operator is not included in the state vector x .

- Further, it is unclear how the emissions are corrected. How can negative emissions be avoided?

We now answered to this remark in "Section 4.2.2. Covariance matrices B and R ": "With such a set-up, in theory, we could obtain negative posterior emissions since the inversion system does not impose a constraint of positivity in the results. Nevertheless, even 100% of uncertainty lead to a prior distribution mostly (>80%) on the positive side. The assimilation of data showing an increase above the background (at the edges of the domain; not shown) further drive the inversion towards positive emissions for both CO and NO_x inversions. In practice, our inversion does not lead to negative posterior emissions (Figure 7b). Spatial and temporal correlations in B would further limit the probability to get negative emissions locally by smoothing the posterior emissions at a spatial scale at which the "aggregated" prior uncertainty is smaller than 100%. However, a positivity constraint should be implemented in future versions of the system."

- Are the emissions optimized for each time step or for the whole assimilation window?

The user can choose the time resolution at which the emissions are optimized. In our illustrations, we now present inversions at 7-day and at 1-day resolutions.

- Are the emissions constant for the simulation time or does the inversion result in correction factors for the emissions?

Indeed, the emissions are inverted, i.e., the inversion results in correction factors for the emissions at the specified time and spatial scales.

- Then, the special treatment of 4D-var for emission factor optimization should be shown, e.g. how the positive definiteness of the correction factors is ensured. The manuscript must be more precise in this context.

We do not agree. We would like to emphasize that the PYVAR-CHIMERE system for inversion is not a 4D-VAR one.

-The calculation of the size of the control vector is erroneous. The vertical dependence of the initial conditions is missing in the calculation.

The vertical dependence is indeed taken into account. The number of components in the control vector has been corrected.

-In the experiment section (section 4) no information on the initial and boundary conditions is given.

We now provide more information about the initial, lateral and top boundary conditions in the new "Section 4.1.2. CHIMERE set-up": "Different climatological values from the LMDZ-INCA global model [Szopa et al., 2008] or from a MACC reanalysis are used to prescribe concentrations at the lateral and top boundaries and the initial atmospheric composition in the domain."

-It should be illustrated to what degree both are changed during the inversion. Further, a comparison or sensitivity test should be shown on what the impact of emission optimization is compared to a joint optimization with initial and boundary conditions.

We choose not to perform such a sensitivity test. We have added text in "Section 4.2.2. Covariance matrices B and R" to explain this choice: "Based on the sensitivity test in Figure 5, the errors assigned to the CO and NO₂ lateral boundary conditions and to their initial conditions are set at 15%. As these errors are significantly lower than those of the emissions and as CO surface concentrations are mainly due to emissions (Figure 4), we assume a small relative influence of the correction of initial and boundary conditions on our results."

-Although the two test cases show a reduction of the difference between the assimilated observation and the analysis, this is not a proof of the successful operation of the data assimilation algorithm. A comparison with independent observations and a table with quality measures (e. g. bias, root mean square error, cost reduction) is necessary.

Indeed, but the main purpose of a GMD paper is less to present specific inversion studies than to describe the general modeling framework. We chose not to present evaluation for our illustration, as this is not the scope of this paper. Nevertheless, we have added sentences about the reduced mean bias between the observations and the simulation using the posterior emissions instead of the prior ones in Section 4.2.3 and in Section 4.2.4 to show the successful operation of the inversion system.

- It is advised to perform the analysis on a few consecutive days to assess the stability and quality of the inversion on different days.

We agree, to assess the stability and quality of the inversion, we now present a period of 7 days for the CO inversion.

- in the description of the test cases both, initial values and boundary conditions are included in the control vector, thus, the analysis is not complete without showing these two variables. A discussion is needed about the correction for all three variables, i.e. emissions, initial values, and boundary conditions, their relative influence on the analysis and about potential limitations of the inversion.

As already explained above, we choose not to perform such a sensitivity test. We have added text in "Section 4.2.2. Covariance matrices B and R" to explain this choice: "Based on the sensitivity test in Figure 5, the errors assigned to the CO and NO₂ lateral boundary conditions and to their initial conditions are set at 15%. As these errors are significantly lower than those of the emissions and as CO surface concentrations are mainly due to emissions (Figure 4), we assume a small relative influence of the correction of initial and boundary conditions on our results."

-If the full adjoint of the chemical processes is used there should be an adjoint signal for other species than CO and NO₂ as well. This must be clarified. Are these signals simply not considered or not discussed? What is the reason for not optimizing NO emissions then?

The adjoint compute the sensitivity to all the components of the x vector. In the inversion we made for the former version of this paper, we chose to only infer NO₂ emissions. As both the reviewers have been disturbed by this illustration, CO, NO and NO₂ are now included in the x vector and we now present inversion for NO_x emissions. Other species could be considered for other studies.

-the model resolution of 0.5 x 0.5 square degrees seems to be a bit coarse for anthropogenic emission assessments. Is nesting available? A discussion on this point is needed.

Yes, nesting is available in CHIMERE. A number of studies for anthropogenic emission assessments have been done at even coarser resolution than 0.5x0.5°: for example, Miyazaki et al. [2017] using an approximately 2.8°x2.8° resolution with the global CTM MIROC-Chem or Wang et al. [2019] using a 2.5° or 2.5° resolution with Geos-Chem.

We discussed about finer resolutions in the perspectives of the study.

Miyazaki, K., Eskes, H., Sudo, K., Boersma, K. F., Bowman, K., and Kanaya, Y.: Decadal changes in global surface NO_x emissions from multi-constituent satellite data assimilation, *Atmos. Chem. Phys.*, 17, 807–837, <https://doi.org/10.5194/acp-17-807-2017>, 2017.

Wang, Y., Wang, J., Xu, X., Henze, D. K., and Qu, Z.: Inverse modeling of SO₂ and NO_x emissions over China using multi-sensor satellite data: 1. formulation and sensitivity analysis, *Atmos. Chem. Phys. Discuss.*, <https://doi.org/10.5194/acp-2019-879>, in review, 2019.

-a better description of the B-matrix is needed in section 4.1.3.

We agree, we have added information about the B-matrix, in Section 3.3: " Different simple but efficient ways of building the error covariance matrix B are implemented in PYVAR-CHIMERE. The variances and correlations are defined independently. The variances are specified by the user through standard deviation coefficient (Table 1), which can be a fixed value ("fx") or a percentage ("pc") to define the diagonal standard deviation matrix Σ . For correction types "mult" and "scale", as well as for correction type "add" with a fixed value, the value is directly used as the standard deviation of the uncertainty in the corresponding components of the control vector. For correction type "add" with a percentage provided, maps of standard deviation of uncertainty are built by applying this percentage to the matching input fields (fluxes, initial conditions, boundary conditions). The user may also provide a script to build personalized maps of variances.

Potential correlations between uncertainties in different types of control variables, e.g. between fluxes and boundary conditions, and correlations between uncertainties in different species, e.g. between fluxes of CO and NO_x, are not coded yet. Only correlations for a given type of control variable and a given species are so far taken into account so that the B matrix is block diagonal. For a given type of control variable and a given species (in the illustration in section 4.2.2: CO, NO or NO₂ fluxes), spatial and temporal correlations can be defined using correlation lengths through time L_t and space L_s . Those lengths are used to model temporal and/or spatial auto-correlations using an exponentially decaying function: the correlation r between parameters and at a given location but separated by duration $d(x_i, x_j)$, or at a given time but distant by $d(x_i, x_j)$ is given by $r(x_i, x_j) = \exp\left(\frac{-d(x_i, x_j)}{L}\right)$ where L ($= L_T$ or L_S) is the corresponding correlation length. There is no correlation between uncertainties in land and

ocean flux. . Note that the spatial correlations are computed for each vertical level independently when dealing with control variables with vertical resolution (3D fields of fluxes when accounting for emission injection heights, or boundary/initial conditions). Vertical correlations in the uncertainties in such variables have not been coded yet. Apart from this, the system assumes that temporal correlations and spatial correlations depend on the time lag and distance but not on the specific time and location of the corresponding parameters. It also assumes that the correlation between uncertainties at different locations and different time can be derived from the product of the corresponding autocorrelation in time and space.

Each block of B can thus be decomposed based on Kronecker products: $B = \sum C_t \otimes C_s \sum$ where \otimes is the Kronecker product, C_t and C_s are the temporal and spatial correlations, respectively. The calculations involving $B^{1/2}$ are simplified in PYVAR-CHIMERE using the Eigen-decomposition of C_t and C_s . Its square root can be calculated according to: $C_t^{1/2} = V_{C_t} D_{C_t}^{1/2} V_{C_t}^T$ (and similarly for C_s) (Eq 4) where V_{C_t} is the matrix with the Eigenvectors as columns, and D_{C_t} is the diagonal matrix of Eigenvalues of C_t . It is possible to chose a threshold under which the eigenvalues are truncated when computing the spatial correlations in order to save computation and memory, but not when computing the temporal correlations."

-What about correlations for initial and boundary conditions?

There is no correlation for initial and boundary conditions in our inversions.

Further minor comments:

- line 30: (VOCs) instead of "(VOCs)"

It has been changed.

-line 39: reference for (LRTAP) would be appreciated

We added the UNECE website as a reference for LRTAP.

-line 43: no commas

The commas have been removed.

- line 85: CO and NOx (instead of "CO, NOx")

It has been changed.

-line 88: citation van der A. [2008] is not appropriate (van der A et al. [2008]), also in the reminder of the manuscript

It has been changed.

-line 93/94: ".. for which variational methods are more suitable than KFs by design": a reference would be appreciated for this statement.

This sentence has been removed.

-line 122/123: of the current inversion (instead "of the inversion")

It has been changed.

-line 163: quasi-Newton (instead "quasi-Newtonian")

It has been changed.

-line 165: Reference for incremental 4D-var approach is appreciated

We would like to emphasize that the PYVAR-CHIMERE system for inversion is not a 4D-VAR one. We do not need reference for incremental 4D-var approach.

- line 203: It would be appreciated if the manuscript contains a table with the available (and adjoint) processes of CHIMERE

The available processes of CHIMERE are already listed in Figure 1 (emissions, transport, chemistry and deposition).

- line 227/228: better: "PYVAR, CHIMERE, and text sources are displayed in blue, orange, and grey boxes, respectively."

It has been changed.

- caption of figure 4: better: "Simplified scheme of how PYVAR scripts prepare the observations y using satellite data. PYVAR and text sources are displayed in blue and grey boxes, respectively."

It has been changed.

- line 264: Equation " $C_m =$ " is not a correct mathematical formulation, $C_m(o)$ is a column, x_a is the state vector (a profile in this context).

Here, $C_m(0)$ is not a column but the vertical distribution in partial subcolumns from a chemistry-transport model at the same satellite pressure levels. x_a is not the state vector but the a priori profile provided together with the averaging kernels when relevant. We kept this formulation.

- line 290: ... days for CO and NO₂, respectively (instead of "... days, respectively for CO and NO₂")

It has been changed.

- line 302: Table 1 is not control vector specific. This sentence can be removed

Indeed, we move this sentence in Section 4.

- line 304: for one day (instead "at a 1-day"); resolution (instead "resolutions")

It has been changed.

- line 313/314: a spin-up for the initial values is needed for an appropriate analysis, otherwise the model maybe to far off the observations for a suitable correction.

We agree, we indeed performed runs with a spin-up of 10 days. We have added this information in "Section 4.1.2. CHIMERE set-up": "In order to ensure realistic fields of simulated CO and NO₂ concentrations from the beginning of the inversion period, runs have been preceded with a 10-day spin-up."

- line 317: Reference for MOPITT is missing

Indeed, we have added a reference.

- line 328: MOPITT instead of "OMI"

It has been changed.

- page 12, line 4: flown instead of "flying"

It has been changed.

- line 368: parts (instead of "part"); present (instead of "presents")

It has been changed.

- page 14, last line: particularly over the Po Valley (instead ", and particularly over PoValley")

It has been changed.

- caption Fig. 7 d: is it really the difference between prior and posterior? Inconsistency with text (see next point)

- line 374: Fig. 5c seems to be wrong here. Is it Fig. 7d?

Indeed, this has been corrected.

- line 380/381: Using the full adjoint of CHIMERE, this must already be available. Please check for adjoint NO signals

As already explained above, we now present inversion of NO_x emissions.

- line 399: remove "for example"

It has been removed.

Variational regional inverse modeling of reactive species emissions

with PYVAR-CHIMERE-v2019

Audrey Fortems-Cheiney¹, Isabelle Pison¹, Grégoire Broquet¹, Gaëlle Dufour², Antoine Berchet¹,
Elise Potier¹, Adriana Coman², Guillaume Siour², and Lorenzo Costantino²

¹Laboratoire des Sciences du Climat et de l'Environnement, LSCE-IPSL (CEA-CNRS-UVSQ),
Université Paris-Saclay, 91191 Gif-sur-Yvette, France.

²Laboratoire Interuniversitaire des Systèmes Atmosphériques, UMR CNRS 7583, Université Paris
Est Créteil et Université Paris Diderot, Institut Pierre Simon Laplace, Créteil, France.

Abstract

Up-to-date and accurate emission inventories for air pollutants are essential for understanding their role in the formation of tropospheric ozone and particulate matter at various temporal scales, for anticipating pollution peaks and for identifying the key drivers that could help mitigate their emissions. This paper describes the Bayesian variational inverse system PYVAR-CHIMERE, which is **now** adapted to the inversion of reactive species, **in addition to greenhouse gases**. Complementarily with bottom-up inventories, this system aims at updating and improving the knowledge on the high spatio-temporal variability of emissions of air pollutants and their precursors. The system is designed to use any type of observations, such as satellite observations or surface station measurements. The potential of PYVAR-CHIMERE is illustrated with inversions of both CO and NO_x emissions in Europe, using the MOPITT and OMI satellite observations, respectively.

1. Introduction

The degradation of air quality is a worldwide environmental problem: 91% of the world's population have breathed polluted air in 2016 according to the World Health Organization (WHO), resulting in 4.2 millions of premature deaths every year [WHO, 2016]. The recent study of Lelieveld et al. [2019] even suggests that the health impacts attributable to outdoor air pollution are substantially higher than previously assumed (with 790,000 premature deaths in the 28 countries of the European Union against the previously estimated 500,000 [EEA, 2018]). The main regulated primary (i.e. directly emitted in the atmosphere) anthropogenic air pollutants are carbon monoxide (CO), nitrogen oxides (NO_x =NO+NO₂), sulfur dioxide (SO₂), ammonia (NH₃), volatile organic compounds (VOCs), and primary particles. These primary air pollutants are precursors of secondary (i.e. produced in the atmosphere through chemical reactions) pollutants such as ozone (O₃) and Particulate Matter (PM), which are also threatening to both human health and ecosystems. Monitoring concentrations and quantifying emissions are still challenging and limit our capability

37 to forecast air quality to warn population and to assess i) the exposure of population to air pollution
38 and ii) the efficiency of mitigation policies.

39

40 Bottom-up (BU) inventories are built in the framework of air quality policies such as The
41 Convention on Long-Range Transboundary Air Pollution (LRTAP, <http://www.unece.org>) for air
42 pollutants. Based on national annual inventories, research institutes compile gridded global or
43 regional, monthly inventories (mainly for the US, Europe and China) with a high spatial resolution
44 (currently regional or city scale inventories are typically finer than $0.1^{\circ} \times 0.1^{\circ}$). These inventories are
45 constructed by combining available (economic) statistics data from different detailed activity
46 sectors with the most appropriate emission factors (defined as the average emission rate of a given
47 species for a given source or process, relative to the unit of activity). It is important to note that the
48 activity data (often statistical data) has an inherent uncertainty and that its reliability may vary
49 between countries or regions. In addition, the emission factors bear large uncertainties in their
50 quantification [Kuenen et al., 2014; EMEP/EEA, 2016; Kurokawa et al., 2013]. Moreover, these
51 inventories are often provided at the annual or monthly scale with typical temporal profiles to build
52 the weekly, daily and hourly variability of the emissions. The combination of uncertain activity
53 data, emission factors and emission timing can be a large source of uncertainties, if not errors, for
54 forecasting or analyzing air quality [Menut et al., 2012]. Finally, since updating the inventories and
55 gathering the required data for a given year is costly in time, manpower and money, only a few
56 institutes have offered estimates of the gaseous pollutants for each year since 2011 (i.e, EMEP
57 updated until the year 2017, MEIC updated until the year 2017 to our knowledge). Nevertheless,
58 using knowledge from inventories and air quality modeling, emissions have been mitigated. For
59 example, from 2010 to nowadays, emissions in various countries have been modified and/or
60 regional trends have been reversed (e.g., the decrease of NO_x emissions over China since 2011 [de
61 Foy et al., 2016]), leading to significant changes in the atmospheric composition. Consequently, the
62 knowledge of precise and updated budgets, together with seasonal, monthly, weekly and daily
63 variations of gaseous pollutants driven, amongst other processes, by the emissions are essential for
64 understanding their role in the formation of tropospheric ozone and PMs at various temporal scales,
65 for anticipating pollution peaks and for identifying the key drivers that could help mitigate these
66 emissions.

67

68 In this context, complementary methods have been developed for estimating emissions using
69 atmospheric observations. They operate in synergy between a chemistry-transport model (CTM) -
70 which links the emissions to the atmospheric concentrations-, atmospheric observations of the
71 species of interest, and statistical inversion techniques. A number of studies using inverse modeling

72 were first carried out for long-lived species such as greenhouses gases (GHGs) (e.g., carbon dioxide
73 CO₂ or methane CH₄) at the global or continental scales [Hein et al., 1997; Bousquet et al. 1999],
74 using surface measurements. Later, following the development of monitoring station networks, the
75 progress of computing power, and the use of inversion techniques more appropriate to non-linear
76 problems, these methods were applied to shorter-lived molecules such as CO. For these various
77 applications (e.g., for CO₂, CH₄, CO), the quantification of sources was solved at the resolution of
78 large regions [Pétron et al., 2002]. Finally, the growing availability and reliability of observations
79 since the early 2000s (in-situ surface data, remote sensing data such as satellite data), the
80 improvement of the global CTMs, of the computational capacities and of the inversion techniques
81 have increased the achievable resolution of global inversions, up to the global transport model grid
82 cells, i.e. typically with a spatial resolution of several hundreds of square kilometers [Stavrakou and
83 Muller, 2006; Pison et al., 2009; Fortems-Cheiney et al., 2011; Hooghiemstra et al., 2012; Yin et
84 al., 2015; Miyazaki et al., 2017, Zheng et al., 2019].

85
86 Today, the scientific and societal issues require an up-to-date quantification of pollutant emissions
87 at a higher spatial resolution than the global one and imply to widely use regional inverse systems.
88 However, although they are suited to reactive species such as CO **and** NO_x, and their very large
89 spatial and temporal variability, they have hardly been used to quantify pollutant emissions. Some
90 studies inferred NO_x [Pison et al., 2007; Tang et al., 2013] and VOC emissions [Koohkan et al.,
91 2013] from surface measurements. Konovalov et al. [2006, 2008, 2010], Mijling et al. [2012, 2013],
92 **van der A et al.** [2008], Lin et al. [2012] and Ding et al. [2017] have also shown that satellite
93 observations are a suitable source of information to constrain the emissions of NO_x. These regional
94 inversions using satellite observations were often based on Kalman Filter (KF) schemes [Mijling et
95 al., 2012, 2013; **Van der A et al.**, 2008; Lin et al., 2012; Ding et al., 2017].

96
97 Here, we present the Bayesian variational atmospheric inversion system PYVAR-CHIMERE for the
98 monitoring of anthropogenic emissions at high spatial resolutions. It takes advantage of the previous
99 developments for the quantification of fluxes of long-lived GHG species such as CO₂ [Broquet et
100 al., 2011] and CH₄ [Pison et al., 2018] at the regional to the local scales, but now solves for reactive
101 species such as CO and NO_x. It has also a better level of robustness, clarity, portability, and
102 modularity than these previous systems .It is based on the Bayesian variational assimilation code
103 PYVAR [Chevallier et al. 2005] and on the regional state-of-the-art CTM CHIMERE, dedicated to
104 the study of regional atmospheric pollution events [Menuet et al., 2013, Mailler et al., 2017].
105 Variational techniques require the adjoint of the model to compute the sensitivity of simulated
106 atmospheric concentrations to corrections of the fluxes. CHIMERE is one of the CTMs possessing

107 its adjoint code (e.g., for global models: **GEOS-CHEM** [Henze et al., 2007], IMAGES [Stavrakou
108 and Muller, 2006], TM5 [Krol et al., 2008], GELKA [Belikov et al., 2016] and LMDz [Chevallier
109 et al., 2005; Pison et al., 2009] ; for limited-area models: CMAQ [Hakami et al., 2007], EURAD-
110 IM [Elbern et al., 2007], RAMS/CTM-4DVAR [Yumimoto et Uno, 2006], **WRF-CO2 4D-Var**
111 **[Zheng et al., 2018]**).

112

113 The principle of variational atmospheric inversion and the configuration of PYVAR-CHIMERE are
114 described in Section 2 and in Section 3, respectively. Details about the forward, **tangent-linear** and
115 adjoint codes of CHIMERE are also given. Then, the potential of PYVAR-CHIMERE is illustrated
116 in Section 4 with the optimization of European CO and NO_x emissions, constrained by observations
117 from the Measurement of Pollution in the Troposphere (MOPITT) and from the Ozone Monitoring
118 Instrument (OMI) satellite instruments, respectively.

119

120 **2. Principle of Bayesian variational atmospheric inversion**

121 The Bayesian variational atmospheric inversion method adjusts a set of control parameters in input
122 of the CTM, including parameters related to the emissions whose estimate is the primary target of
123 the inversion. The control vector \mathbf{x} contains these variables to be optimized during the inversion
124 process (surface fluxes but it may also include initial or boundary conditions for example, see
125 Section 3.3). The adjustments are applied to prior values, usually taken, for the emissions, from pre-
126 existing BU inventories. The principle is to minimize, on the one hand, the departures from the
127 prior estimates of the control parameters, which are weighted by the uncertainties in these estimates
128 (called hereafter “prior uncertainties”), and, on the other hand, the differences between simulated
129 and observed concentrations, which are weighted by all other sources of uncertainties explaining
130 these differences (called hereafter all together “observation errors”). In statistical terms, the
131 inversion searches for the most probable estimate of the control parameters given their prior
132 estimates, the observations, the CTM and the associated uncertainties. The solution, which will be
133 called posterior estimate in the following, is found by the iterative minimization of a cost function J
134 [Talagrand et al., 1997], defined as:

$$135 J(\mathbf{x}) = (\mathbf{x} - \mathbf{x}_b)^T \mathbf{B}^{-1}(\mathbf{x} - \mathbf{x}_b) + (H(\mathbf{x}) - \mathbf{y})^T \mathbf{R}^{-1}(H(\mathbf{x}) - \mathbf{y}) \quad (\text{Eq. 1})$$

136

137 H is the non-linear observation operator that projects the state vector \mathbf{x} onto the observation space.
138 In most of the variational atmospheric inversion cases (such as those described in Section 4), the
139 observation operator includes the CTM and an interpolation or an extraction and averaging of the
140 simulated concentration fields (see Section 3.4). The observations in \mathbf{y} could be surface
141 measurements and/or remote sensing data such as satellite data. The prior uncertainties and the

142 observation errors are assumed to be centered and to have a Gaussian distribution. Consequently,
143 the prior uncertainties are characterized by their covariance matrix \mathbf{B} and the observation errors are
144 characterized by their covariance matrix \mathbf{R} . By definition, the observation errors combine errors in
145 both the data and the observation operator, in particular measurement errors and errors in the
146 conversion of satellite measurement into concentration data, errors from the CTM, representativity
147 errors due to the comparison between point measurements and gridded models or due to the
148 representation of the fluxes as gridded maps at a given spatial resolution, and aggregation errors
149 associated with the **optimization** of emissions at a given spatial and/or temporal resolution (**as**
150 **specified in the control vector**) that is different from (usually coarser than) that of the CTM [Wang
151 et al., 2017].

152

153 For inversions with observation and control vectors having a high dimension, the minimum of J
154 cannot be found analytically due to computational limitations. It can be reached iteratively with a
155 descent algorithm. In this case, the iterative minimization of J is based on a gradient method. J is
156 calculated with the forward observation operator (including the CTM) and its gradient relative to
157 the control parameters \mathbf{x} : $\nabla J(\mathbf{x}) = \mathbf{B}^{-1}(\mathbf{x} - \mathbf{x}_b) + H^T \mathbf{R}^{-1}(H(\mathbf{x}) - \mathbf{y})$ (Eq. 2) is provided by the
158 adjoint of the observation operator (including the adjoint of the CTM). As shown in Figure 1, the
159 minimization algorithm repeats the forward-adjoint cycle to seek an optimal solution for the control
160 parameters.

161

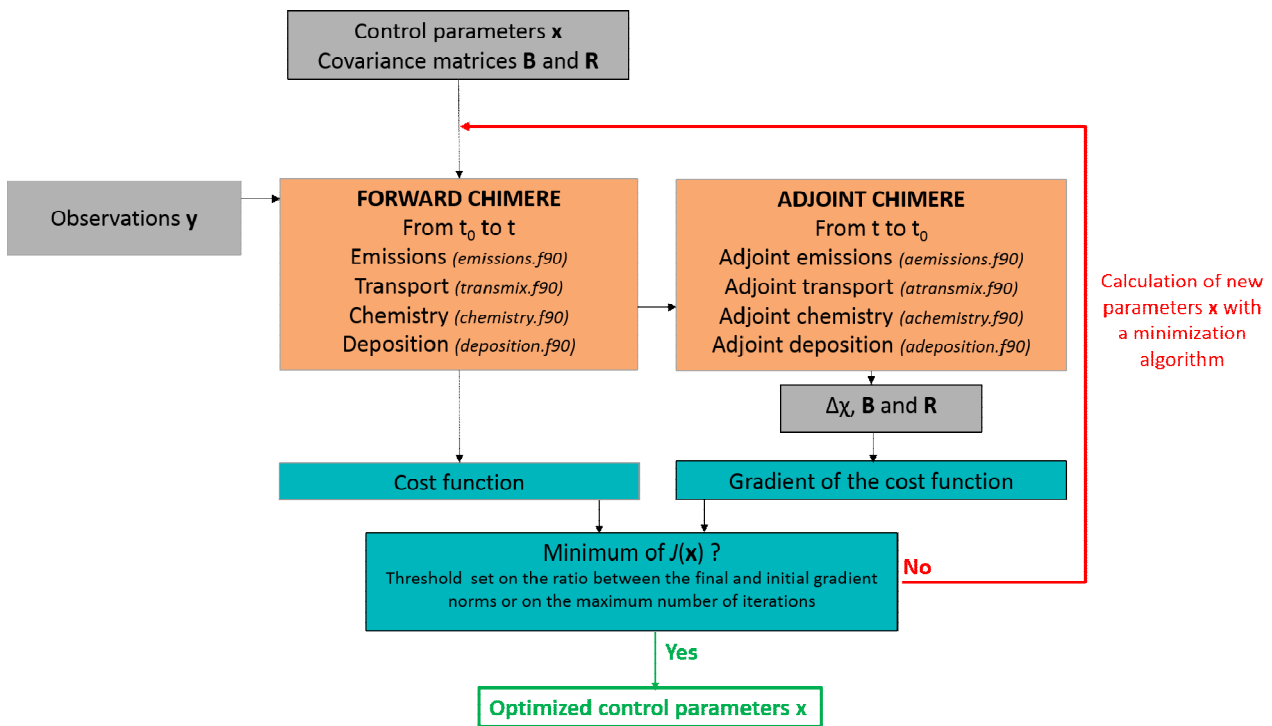
162 **The high-non linearity of the chemistry for reactive species makes it difficult to use its**
163 **tangent-linear to approximate the actual observation operator (e.g. as in Chevallier et al.**
164 **[2010] who use the conjugate gradient algorithm of Fisher and Courtier [1995]), and, more**
165 **generally, it makes the inversion problem highly non linear.** Therefore, in PYVAR-CHIMERE,
166 we use the M1QN3 limited memory quasi-Newton minimization algorithm [Gilbert and
167 Lemaréchal, 1989], which relies on the actual CHIMERE non-linear model to compute J at each
168 iteration of the minimization. As most **quasi-Newton** methods, it requires an initial regularization
169 of \mathbf{x} , the vector to be optimized, for better efficiency. We adopt the most generally used
170 regularization, made by minimizing in the space defined by $\chi = \mathbf{B}^{\frac{1}{2}}(\mathbf{x} - \mathbf{x}_b)$ instead of the control
171 space defined by \mathbf{x} . Although more advanced regularizations can be chosen, the minimization with χ
172 is preferred for its simplifying the equation to solve. In the χ -space, Equation 2 can be re-written as
173 follows: $\nabla J\chi = \chi + \mathbf{B}^{\frac{1}{2}}H \times (\mathbf{R}^{-1}(H(\mathbf{x}) - \mathbf{y}))$. The criterion for stopping the algorithm is based on
174 a threshold set on the ratio between the final and initial gradient norms or on the maximum number

175 of iterations to perform. Due to the non-linearity of the problem, the minimization may reach only a
 176 local minimum.

177

178 Finally, the calculation of the uncertainty in the estimate of emissions from the inversion, known as
 179 “posterior uncertainty”, is challenging in a variational inverse system. Even though the posterior
 180 uncertainty can be explicitly written in various analytical forms, it requires the inversion of matrices
 181 that are too large to invert given the current computational resources in our variational approach. As
 182 a trade-off between computing resources and comprehensiveness, the analysis error may be
 183 evaluated by an approach based on a propagation of errors through sensitivity tests (e.g., as in
 184 Fortems-Cheiney et al., [2012]). It can also be estimated through a Monte Carlo Ensemble
 185 [Chevallier et al., 2007], implemented in PYVAR.

186



187

188 **Figure 1.** Simplified scheme of the iterative minimization in PYVAR-CHIMERE. PYVAR,
 189 CHIMERE and text sources are displayed in blue, in orange and in grey, respectively.

190

191 3. The PYVAR-CHIMERE configuration

192 3.1. PYVAR adapted to CHIMERE

193 The PYVAR-CHIMERE inverse modeling system is based on the Bayesian variational assimilation
 194 code PYVAR [Chevallier et al. 2005] and on a previous inversion system coupled to CHIMERE
 195 [Pison et al., 2007]. PYVAR is an ensemble of Python scripts, which deals with preparing the
 196 vectors and the matrices for the inversion, drives the required Fortran codes of the transport model
 197 and computes the minimization of the cost function to solve the inversion. Previously used for
 198 global inversions with the LMDz model (e.g., Pison et al., 2009; Chevallier et al., 2010; Fortems-

199 Cheiney et al., 2011; Yin et al., 2015; Locatelli et al., 2015; Zheng et al., 2019), **PYVAR has been**
200 **adapted to CHIMERE with an adjoint code without chemistry a first time by Broquet et al.**
201 **[2011]. In order to couple PYVAR to the new state-of-the-art version of CHIMERE (see**
202 **Section 3.2), to include chemistry, and to increase its modularity, flexibility and clarity, the**
203 **new system described here has been developed. It includes elements of the inversion system**
204 **(coded in Fortran90) of [Pison et al., 2007].**
205

206 **3.2. Development and parallelization of the adjoint and tangent-linear codes of** 207 **CHIMERE**

208 To compute the sensitivity of simulated atmospheric concentrations to corrections to the fluxes, the
209 adjoint of CHIMERE has been developed. Originally, the sequential adjoint was coded [Menut et
210 al., 2000; Menut et al., 2003; Pison et al., 2007]. The adjoint has been coded by hand line by line,
211 following the principles formulated by Talagrand [1997]. It contains exactly the same processes as
212 the CHIMERE forward model. **Then, it has been parallelized. This work required a redesigning**
213 **of the whole code, associated with a full testing scheme. Furthermore, the tangent-linear (TL)**
214 **code has been developed and validated at LSCE. Changes have been implemented in the**
215 **forward CHIMERE code embedded in PYVAR-CHIMERE to match requirements of the**
216 **studies lead with PYVAR-CHIMERE. These changes have been implemented in both the**
217 **adjoint and the TL codes. Compared to the CHIMERE 2013 version [Menut et al., 2013], the**
218 **most important of these changes are:**

- 219 **•For the geometry, the possibility of polar domains and the use of the coordinates of the**
220 **corners of the cells instead of only the centers**
- 221 **•For the transport, the non-uniform Van Leer transport scheme on the horizontal,**
- 222 **•For chemistry, various switches have been added to avoid going into the chemistry,**
223 **deposition and wet deposition routines when no species requires them (e.g. no chemistry for**
224 **methane at a regional scale).**

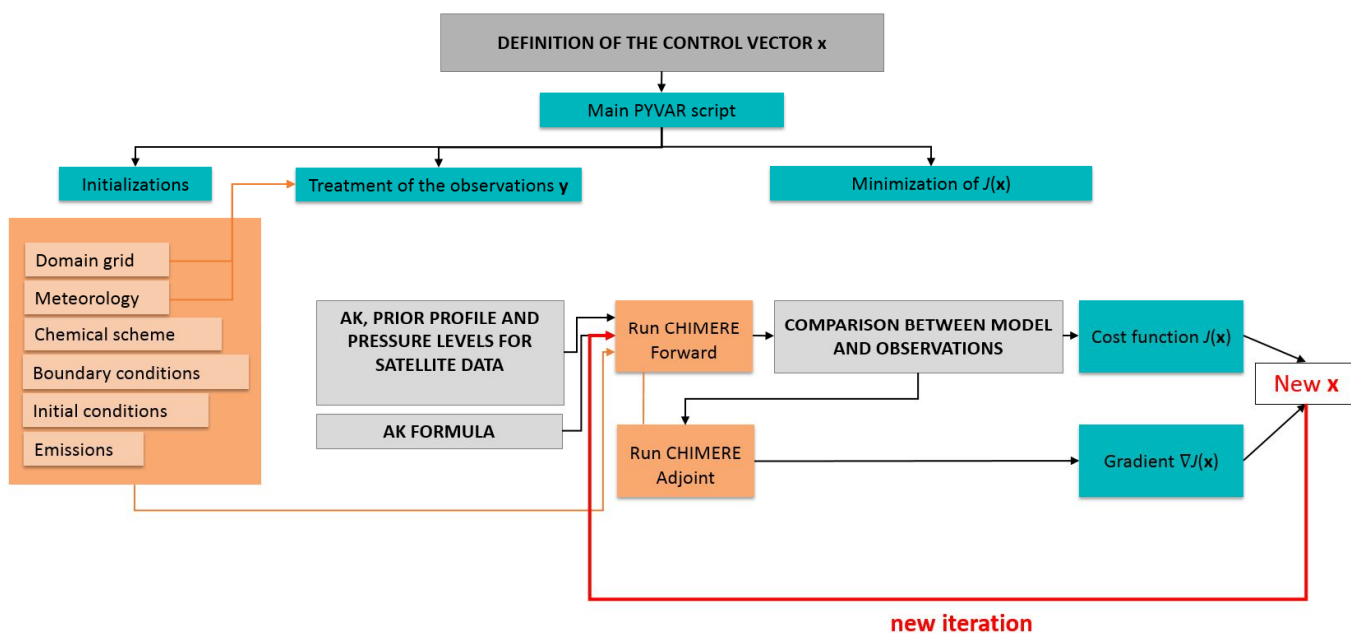
225
226 PYVAR-CHIMERE is currently operational for the full module of gaseous chemistry. As a
227 compromise between the robustness of the method for reactive species, the time required coding the
228 adjoint and the computational cost with a full chemical scheme, the aerosols modules of CHIMERE
229 have not been included in the adjoint of CHIMERE yet and are therefore not available in PYVAR-
230 CHIMERE. The development and maintenance of the adjoint means that the version used is
231 necessarily one or two versions behind the distributed CHIMERE version
232 (<http://www.lmd.polytechnique.fr/chimere/>). **It should also be noted that PYVAR-CHIMERE**
233 **only infer anthropogenic emissions at this stage. The optimization of biogenic emissions,**

234 which are linearly interpolated at the sub-hourly scale in CHIMERE, is currently under
 235 development.

236

237 As an example, Figure 2 presents a simplified scheme of how PYVAR scripts are used to drive this
 238 version of CHIMERE for forward simulations and inversions using satellite observations. A mode
 239 is also available to test the adjoint: it runs the TL code.

240



241

242 **Figure 2.** Simplified scheme of how PYVAR scripts are used to drive CHIMERE for an inversion
 243 using satellite observations. PYVAR, CHIMERE and text sources are displayed in blue, in orange
 244 and in grey, respectively. “AK” refers to Averaging Kernels as detailed in Section 3.4.

245

246 3.3. Definition of the control vector

247 The control vector is specified by the user in a text file. This file is formatted following Table 1. The
 248 parameters to constrain could be fluxes and/or initial conditions and/or boundary concentration
 249 conditions, at the grid-cell resolution or for one region encompassing up to the whole domain.
 250 Several types of corrections can be applied, they are defined in the code as "add", "mult" or
 251 "scale". Both the corrections "add" and "mult" are applied to gridded control variables. For
 252 correction type “add” the control variables are increments added to the corresponding
 253 components of the model inputs. For correction type “mult”, the control variables are scaling
 254 factors multiplying the corresponding components of the model inputs. The difference
 255 between the two options "add" and "mult" plays a role when inverting fluxes which can
 256 switch from positive to negative values (like CO₂ natural fluxes). For type “scale”, the
 257 corrections consist in applying scaling factors to activity maps and/or masks for regions

258 (which is similar to the control of budgets for different regions, types of activities, and/or
259 processes in inversions where the control vector is not gridded [Wang et al., 2018]) and adding
260 the obtained values to the corresponding components of the model inputs.

261 Different simple but efficient ways of building the error covariance matrix B are implemented
262 in PYVAR-CHIMERE. The variances and correlations are defined independently. The
263 variances are specified by the user through standard deviation coefficient (Table 1), which
264 can be a fixed value ("fx") or a percentage ("pc") to define the diagonal standard deviation
265 matrix Σ . For correction types "mult" and "scale", as well as for correction type "add" with
266 a fixed value, the value is directly used as the standard deviation of the uncertainty in the
267 corresponding components of the control vector. For correction type "add" with a percentage
268 provided, maps of standard deviation of uncertainty are built by applying this percentage to
269 the matching input fields (fluxes, initial conditions, boundary conditions). The user may also
270 provide a script to build personalized maps of variances.

271

272 Potential correlations between uncertainties in different types of control variables, e.g.
273 between fluxes and boundary conditions, and correlations between uncertainties in different
274 species, e.g. between fluxes of CO and NO_x, are not coded yet. Only correlations for a given
275 type of control variable and a given species are so far taken into account so that the B matrix
276 is block diagonal. For a given type of control variable and a given species (in the illustration in
277 section 4.2.2: CO, NO or NO₂ fluxes), spatial and temporal correlations can be defined using
278 correlation lengths through time L_t and space L_s . Those lengths are used to model temporal
279 and/or spatial auto-correlations using an exponentially decaying function: the correlation r
280 between parameters and at a given location but separated by duration $d(x_i, x_j)$, or at a given
281 time but distant by $d(x_i, x_j)$ is given by $r(x_i, x_j) = \exp\left(\frac{-d(x_i, x_j)}{L}\right)$ where L ($= L_T$ or L_S) is the
282 corresponding correlation length. There is no correlation between uncertainties in land and
283 ocean flux. Note that the spatial correlations are computed for each vertical level
284 independently when dealing with control variables with vertical resolution (3D fields of fluxes
285 when accounting for emission injection heights, or boundary/initial conditions). Vertical
286 correlations in the uncertainties in such variables have not been coded yet. Apart from this,
287 the system assumes that temporal correlations and spatial correlations depend on the time lag
288 and distance but not on the specific time and location of the corresponding parameters. It also
289 assumes that the correlation between uncertainties at different locations and different time
290 can be derived from the product of the corresponding autocorrelation in time and space.

291 Each block of B can thus be decomposed based on Kronecker products: $B = \sum C_t \otimes C_s \sum$ where
 292 \otimes is the Kronecker product, C_t and C_s are the temporal and spatial correlations, respectively.
 293 The calculations involving $B^{1/2}$ are simplified in PYVAR-CHIMERE using the Eigen-
 294 decomposition of C_t and C_s . Its square root can be calculated according to: $C_t^{1/2} =$
 295 $V_{C_t} D_{C_t}^{1/2} V_{C_t}^T$ (and similarly for C_s) (Eq 4) where V_{C_t} is the matrix with the Eigenvectors as
 296 columns, and D_{C_t} is the diagonal matrix of Eigenvalues of C_t . It is possible to chose a threshold
 297 under which the eigenvalues are truncated when computing the spatial correlations in order
 298 to save computation and memory, but not when computing the temporal correlations.

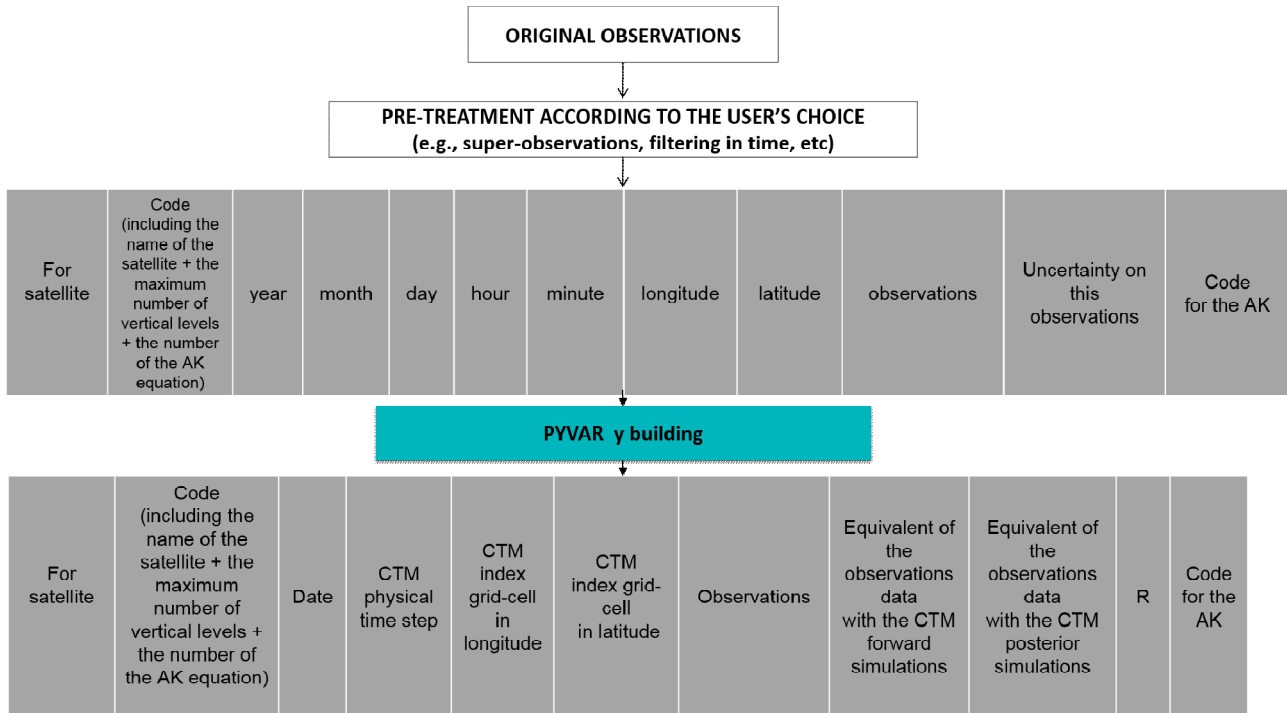
Possible ways to define the control vector and to construct the error covariance B matrix								
Constrained species	Correction type : - Add - Mult - Scale	Spatial resolution - at the grid-cell resolution - for one region	Temporal resolution (in hours)	Input to constrain: -Fluxes -Initial conditions -Lateral Boundary conditions -Top Boundary conditions	B variance coefficient: -fx -pc	Decorrelation time (in hours)	Decorrelation length on land (in km)	Decorrelation length on sea (in km)
Examples of the definition of the control vector and of the construction of the B matrix for the experiments presented in Section 4								
CO	add	0.5°x0.5°	24	Fluxes	100 %	-	-	-
CO	add	0.5°x0.5°	24	Initial conditions	15%	-	-	-
CO	add	0.5°x0.5°	24	Lateral Boundary conditions	15%	-	-	-
CO	add	0.5°x0.5°	24	Top Boundary conditions	15%	-	-	-
NO	add	0.5°x0.5°	24	Fluxes	30 %	-	50	50
NO	add	0.5°x0.5°	24	Initial conditions	15%	-	-	-
NO ₂	add	0.5°x0.5°	24	Fluxes	30 %	-	50	50
NO ₂	add	0.5°x0.5°	24	Initial conditions	15%	-	-	-

299 **Table 1.** Possible ways to define the control vector and to construct the error covariance B matrix
 300 in PYVAR-CHIMERE and examples of the configuration for the experiments presented in Section 4.

301 3.4 Equivalents of the observations

302 The individual data given as constraints in the system are first formatted into a text file described in
 303 Figure 4. During forward simulations, the equivalents of the components of y (i.e, the equivalents

304 of the individual data) are calculated by PYVAR-CHIMERE. It includes the CTM and an
 305 interpolation (see below the vertical interpolation from the model's grid to the satellite levels) or an
 306 extraction and averaging (e.g. extracting the grid cell matching the geographical coordinates of a
 307 surface station and averaging over one hour). As a compromise between technical issues such as the
 308 time required for reading/writing files, the observation operator H that generates the equivalent of
 309 the observations by the model (i.e. $H(\mathbf{x})$) has been so far partly embedded in the code of CHIMERE.
 310 It makes it easier to use finer time intervals than available in the usual hourly outputs of CHIMERE
 311 to compute the required information (e.g., within the finer CTM physical time steps).



312
 313 **Figure 3.** Simplified scheme of how PYVAR scripts prepares the observations, using satellite data
 314

315 To make comparisons between simulations and satellite observations, the simulated vertical profiles
 316 are first interpolated on the satellite's levels (with a vertical interpolation on pressure levels) in
 317 **CHIMERE**. Then, the averaging kernels (AKs), when available, are applied to represent the
 318 vertical sensitivity of the satellite retrieval. Two types of formula, depending on the satellite
 319 observations used, have been detailed in PYVAR-CHIMERE for the use of AKs: $C_m = AK \cdot C_{m(o)}$
 320 or $C_m = x_a + AK(C_{m(o)} - x_a)$ where C_m is the modeled column, AK contains the averaging
 321 kernels, x_a is the prior profile (provided together with the AKs when relevant) and $C_{m(o)}$ is the
 322 vertical distribution of the original model partial columns interpolated to the pressure grid of the
 323 averaging kernels.

324
 325 **3.5. Numerical language**

326 The PYVAR code is in Python 2.7, the CHIMERE CTM is coded in Fortran90. The CTM requires
 327 several numerical tools, compilers and libraries. The **PYVAR-CHIMERE system** was developed
 328 and tested using the software versions as described in Table 2.
 329

		URL	Version
Software	Python	https://www.python.org/downloads/	2.7
	Fortran compiler ifort	https://software.intel.com/en-us/fortran-compilers	Composer-xe- 2013.2.146
Libraries or packages	UnidataNetCDF	https://www.unidata.ucar.edu/	3
	Open MPI	https://www.open-mpi.org/	1.10.5
	GRIB_API	https://confluence.ecmwf.int/display/GRIB/Releases	1.14
	nco	http://nco.sourceforge.net/#Source	4.6.3

330 **Table 2.** URL addresses for the development and the use of the PYVAR-CHIMERE system and its
 331 modules.

332
 333 PYVAR-CHIMERE’s computation time for one node of 10 CPUs is about 4h for 1 day of inversion
 334 (with ~10 iterations) for the European domain size of 101 (longitude) x 85 (latitude) x 17 (vertical
 335 levels) used in Section 4.2.3. The model parallelism results from a Cartesian division of the main
 336 geographical domain into several sub-domains, each one being processed by a worker process. To
 337 configure the parallel sub-domains, the user has to specify two parameters in the model parameter
 338 file: the number of sub-domains for the zonal and meridian directions. The total number of CPUs
 339 used is therefore the product of these two numbers plus one for the master process.

340 341 **4. Potential of PYVAR-CHIMERE for the inversion of CO and NO_x emissions**

342 The potential of the PYVAR-CHIMERE system to invert emissions of reactive species is illustrated
 343 with the inversion of CO and NO_x **anthropogenic** emissions in Europe respectively based on
 344 MOPITT CO data and OMI NO₂ data. We have chosen to present illustration of CO inversion **over**
 345 **a 7-day window, the first week of March 2015. Considering the short lifetime of NO_x of a few**
 346 **hours [Valin et al., 2013; Liu et al., 2016],** we have chosen to present illustration of NO_x inversion
 347 over a 1-day window, the 19th February 2015. These particular periods have been chosen as they
 348 present **a representative** number of super-observations during winter, and as the emissions are high
 349 during that period. All the information required by the system to invert CO and NO_x emissions are
 350 listed in Table 1.

351 352 **4.1. Data and model description** 353 **4.1.1. Observations y**

354 We use CO data from the MOPITT instrument [Deeter et al., 2019]. MOPITT has been flown
355 onboard the NASA EOS-Terra satellite, on a low sun-synchronous orbit that crosses the equator at
356 10:30 and 22:30 LST. The spatial resolution of its observations is about $22 \times 22 \text{ km}^2$ at nadir. It has
357 been operated nearly continuously since March 2000. MOPITT CO products are available in three
358 variants: thermal-infrared TIR only, near-infrared NIR only and the multispectral TIR-NIR product,
359 all containing total columns and retrieved profiles (expressed on a ten-level grid from the surface to
360 100 hPa). We choose to constrain CO emissions with the MOPITT surface product for our
361 illustration. Among the different MOPITTv8 products, we choose to work with the multispectral
362 MOPITTv8-NIR-TIR one, as it provides the highest number of observations, with a good
363 evaluation against in situ data from NOAA stations [Deeter et al., 2019]. The MOPITTv8-NIR-TIR
364 surface concentrations are sub-sampled into “super-observations” in order to reduce the effect of
365 errors that are correlated between neighboring observations: we selected the median of each subset
366 of MOPITT data within each $0.5^\circ \times 0.5^\circ$ grid-cell and each physical time step (about 5-10 minutes).
367 After this screening, 8437 “super-observations” remain in the 7-day inversion (from 10667 raw
368 observations). These super-observations are provided to PYVAR-CHIMERE as constraints \mathbf{y} , and
369 treated as described in Section 3.4. It is important to note that the potential of **MOPITT** to provide
370 information at a high temporal resolution, up to the daily scale, is hampered by the cloud coverage
371 (see the blanks in Figure 6b).

372

The observational constraint on NO_2 emissions comes from the OMI QA4ECV tropospheric columns [Muller et al., 2016; Boersma et al., 2016, Boersma et al., 2017]. The Ozone Monitoring Instrument (OMI), a near-UV/Visible nadir solar backscatter spectrometer, was launched onboard EOS Aura in July 2004. It has been **flown** on a 705 km sun-synchronous orbit that crosses the Equator at 13:30 LT. Our data selection follows the criteria of the OMI QA4ECV data quality statement. As the spatial resolution of the OMI data is finer than that of the chosen CHIMERE model grid ($13 \times 24 \text{ km}^2$ against $0.5^\circ \times 0.5^\circ$, respectively), the OMI tropospheric columns are sub-sampled into “super-observations” (median of the OMI data within the $0.5^\circ \times 0.5^\circ$ grid-cell and each physical time step and its corresponding AK).

373

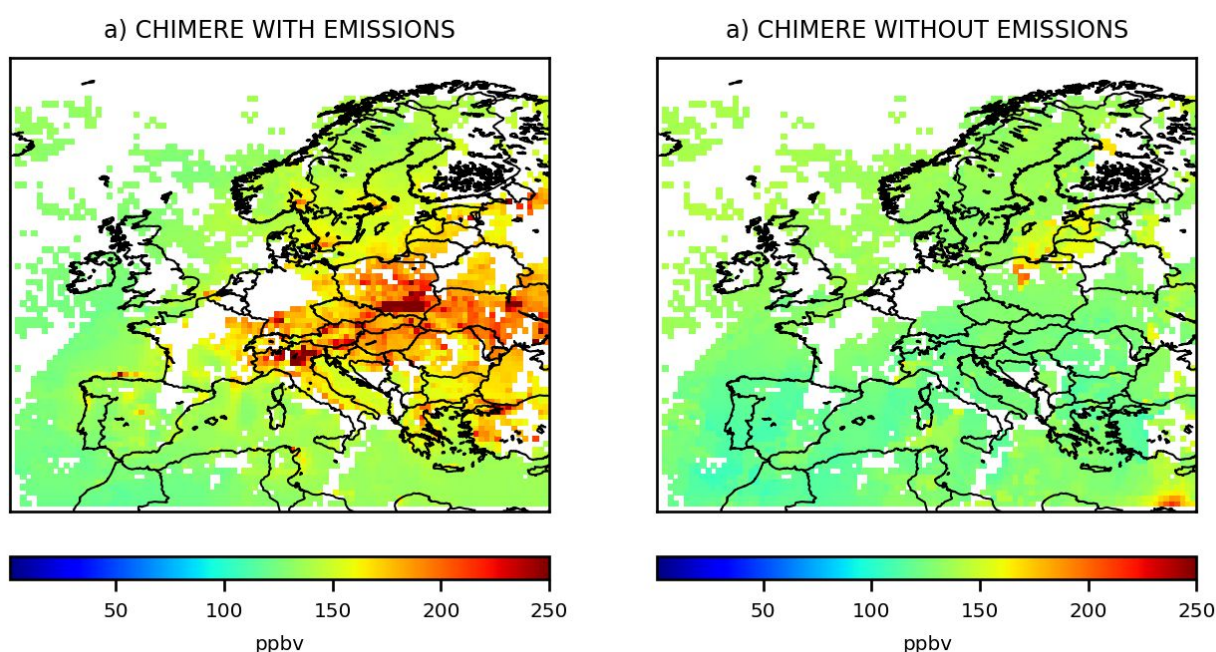
4.1.2 CHIMERE set-up

374 CHIMERE is run over a $0.5^\circ \times 0.5^\circ$ regular grid (about $50 \times 50 \text{ km}^2$) and 17 vertical layers, from the
375 surface to 200hPa (about 12km), with 8 layers within the first two kilometers. The domain includes
376 101 (longitude) x 85 (latitude) grid-cells (15.5°W - 35°E ; 31.5°N - 74°N , see Figure 5). CHIMERE is
377 driven by the **European Centre for Medium-Range Weather Forecasts (ECMWF)**
378 meteorological forecast [Owens and Hewson, 2018]. The chemical scheme used in PYVAR-

379 CHIMERE is MELCHIOR-2, with more than 100 reactions [Lattuati, 1997; CHIMERE 2017],
380 including 24 for inorganic chemistry. **The prior anthropogenic emissions for CO and NO_x**
381 **emissions come from the TNO-GCHco-v1 inventory [Super et al., 2019], the last update of the**
382 **TNO-MACCII inventory [Kuenen et al., 2014]. The prior anthropogenic emissions for VOCs**
383 **come from the EMEP inventory [Vestreng et al., 2005; EMEP/CEIP website]. Different**
384 **climatological values from the LMDZ-INCA global model [Szopa et al., 2008] or from a**
385 **MACC reanalysis are used to prescribe concentrations at the lateral and top boundaries and**
386 **the initial atmospheric composition in the domain. Full access to and more information about**
387 **the MACC reanalysis data can be obtained through the MACC-II web**
388 **site(<http://www.copernicus-atmosphere.eu>). In order to ensure realistic fields of simulated CO**
389 **and NO₂ concentrations from the beginning of the inversion period, runs have been preceded**
390 **with a 10-day spin-up.**

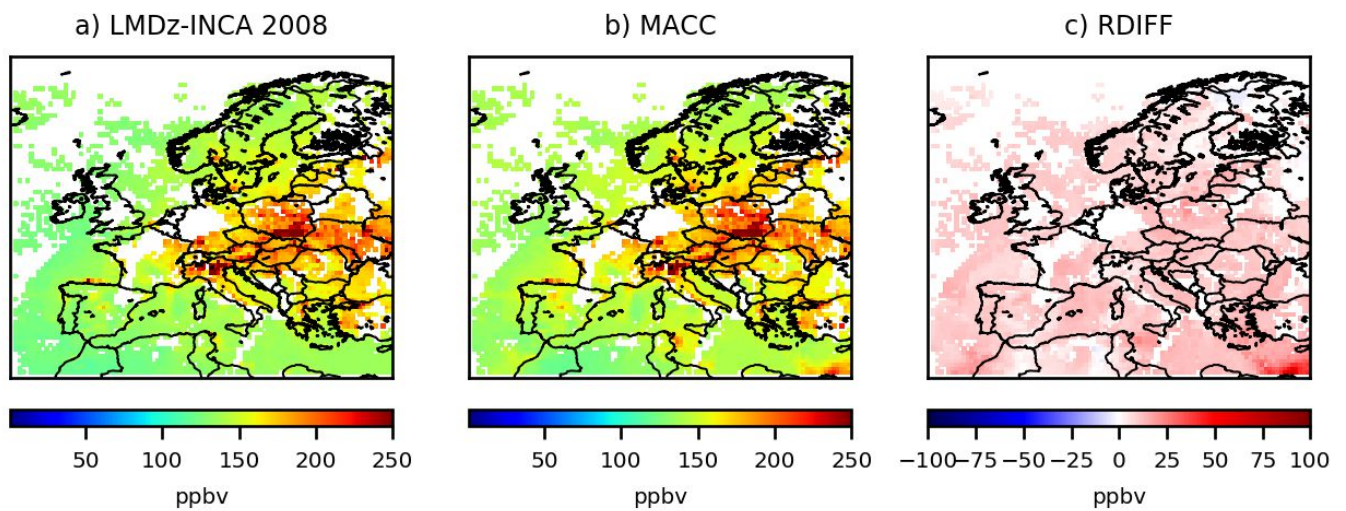
4.1.3. Sensitivity to emissions and to initial and boundary conditions

391 **With its lifetime of about two months, CO could be strongly driven by the initial and lateral**
392 **boundary conditions prescribed in the CTM. In fact, as seen in Figure 4b, initial and**
393 **boundary conditions provide a relatively flat background and the patterns which appear**
394 **clearly over the background are linked to surface emissions (Figure 4a). To characterize the**
395 **uncertainties in the concentration fields due to the initial and lateral boundary conditions, we**
396 **performed a sensitivity test by using either climatological values from LMDZ-INCA or a**
397 **MACC reanalysis: the results were not significantly different, with relative differences in**
398 **concentrations of less than 15% over continental land (Figure 5c).**



399

Figure 4. CO surface concentrations simulated by CHIMERE a) with anthropogenic and biogenic emissions, and b) without emissions, in ppbv, at the 0.5°x0.5° grid-cell resolution, over Europe averaged from the 1st to the 7th, March 2015.

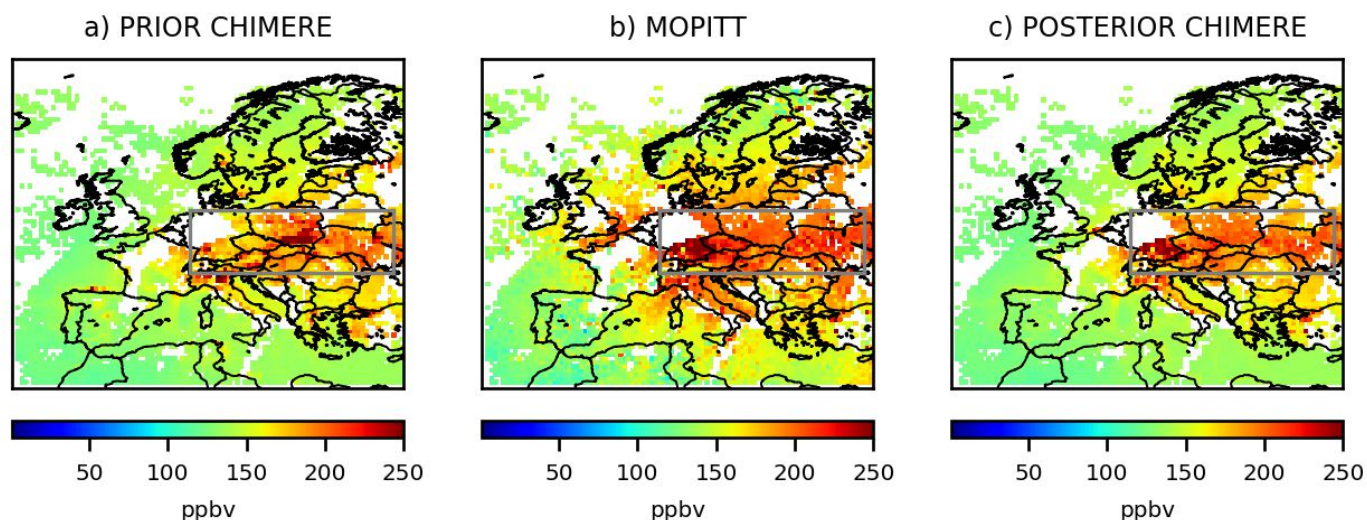


400

Figure 5. CO surface concentrations simulated by CHIMERE using for initial and boundary conditions, a) the climatological values from the LMDZ-INCA global model b) the climatological values from a MACC reanalysis, in ppbv, and c) the relative differences between these two simulations, in %, at the 0.5°x0.5° grid-cell resolution, over Europe averaged from the 1st to the 7th, March 2015.

4.1.4. Comparison between CHIMERE and the observations

401 Large discrepancies are found between the MOPITT CO observations (Figure 6b) and the prior
 402 simulation of their equivalents by CHIMERE over Europe (Figure 6a). For the first week of March
 403 2015, CO concentrations are generally under-estimated by CHIMERE, particularly over Central and
 404 Eastern Europe (excepted in the south of Poland). **On the contrary, CO concentrations seems to**
 405 **be over-estimated over Spain and Portugal.** Large discrepancies are also found between the OMI
 406 NO₂ super-observations and the prior simulation of their equivalents by PYVAR-CHIMERE
 407 (Figure 7). Over Europe, the prior simulation strongly underestimates the tropospheric columns
 408 over industrial areas (e.g., over the Netherlands and over Po Valley). These discrepancies might be
 409 explained by an underestimation in the BU inventory due to a general trend in emissions (if the
 410 underestimation persists throughout the year) or to an underestimation regarding particular activity
 411 sectors or the time profiles at given scales (daily, monthly). This can also be explained by
 412 uncertainties from the satellite data or from the CTM (e.g., atmospheric production, chemistry with
 413 OH).



415

Figure 6. *CO collocated surface concentrations a) simulated by CHIMERE using the prior TNO-GHGco-v1 emissions and the climatological values from the LMDZ-INCA global model for initial and boundary conditions, b) observed by MOPITTv8-NIR-TIR and c) simulated by CHIMERE using the posterior emissions, in ppbv, at the $0.5^\circ \times 0.5^\circ$ grid-cell resolution, over Europe averaged from the 1st to the 7th, March 2015. Mean bias between simulations and observations are given in Section 4.2.3 for the area in the grey box.*

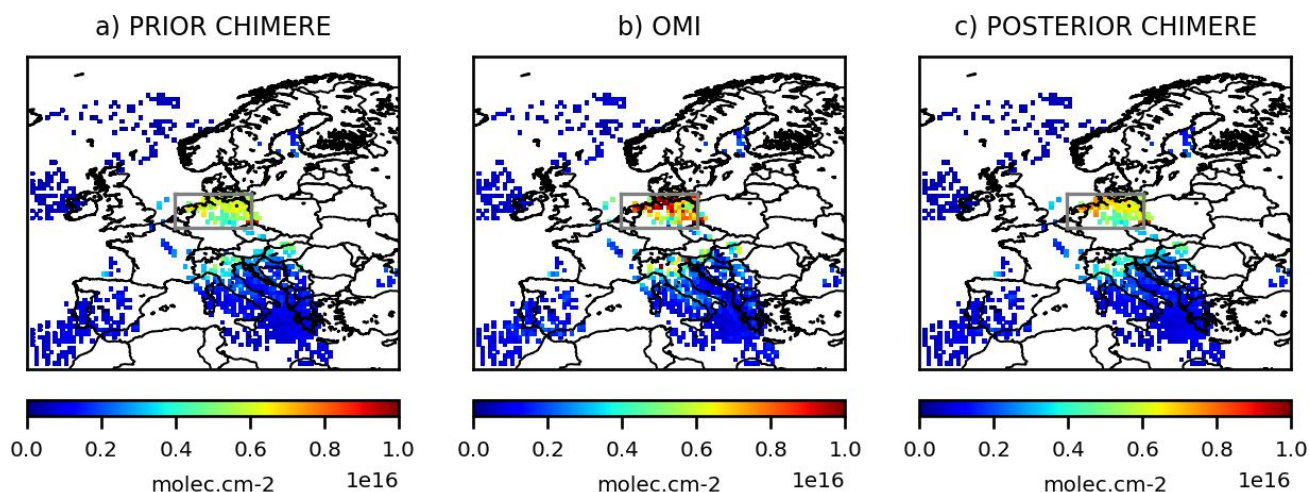


Figure 7. *NO₂ collocated surface concentrations a) simulated by CHIMERE using the prior TNO-GHGco-v1 emissions and the climatological values from the LMDZ-INCA global model for initial and boundary conditions, b) observed by OMI and c) simulated by CHIMERE using the posterior emissions, in $1e^{16}$ molec.cm-2, at the $0.5^\circ \times 0.5^\circ$ grid-cell resolution, over Europe the 19th, February 2015. Mean bias between simulations and observations are given in Section 4.2.4 for the area in the grey box.*

416 4.2. Inversions

417 4.2.1. Control vector x

418 For the CO inversion, the control vector x contains:

- 419 ■ the CO anthropogenic emissions for 7-day and at a $0.5^\circ \times 0.5^\circ$ (longitude, latitude)
420 resolution \times 8 vertical levels, i.e. $101 \times 85 \times 8$ grid cells,
- 421 ■ the CO 3D initial conditions at a $0.5^\circ \times 0.5^\circ$ (longitude, latitude) resolution \times 17 vertical
422 levels,
- 423 ■ the CO lateral and top boundary conditions for 7-day at a $0.5^\circ \times 0.5^\circ$ (longitude,
424 latitude) resolution, i.e. $(2 \times 101 + 2 \times 85) \times 17$ vertical levels.

425 **Considering its short lifetime, there is no boundary conditions for NO_2 .** For the NO_x inversion,
426 the control vector x contains:

- 427 ■ the NO and NO_2 anthropogenic emissions for 1-day and at a $0.5^\circ \times 0.5^\circ$ (longitude,
428 latitude) resolution \times 8 vertical levels, i.e. $101 \times 85 \times 8$ grid cells,
- 429 ■ the NO and NO_2 3D initial conditions at a $0.5^\circ \times 0.5^\circ$ (longitude, latitude) resolution \times
430 17 vertical levels.

431

432 4.2.2. Covariance matrices B and R

433 We hardly have sources of estimates of the uncertainties in bottom-up emission inventories at
434 the 0.5° resolution. The characterization of their statistics in the inversion configuration is
435 consequently often linked with crude assumptions from the inverse modelers. In the NO_x
436 inversions, for both the prior NO and NO_2 emissions at 1-day and 0.5° resolution, the prior
437 error standard deviations is assigned to 30% of the prior estimate of the emissions. As
438 indicated in Section 3.3 and in Table 1, it is possible to use correlations in B, as in Broquet et
439 al., [2011], in Broquet et al., [2013] and in Kadygrov et al., [2015]. For this NO_x illustration,
440 spatial correlations are defined by an e-folding length of 50km over land and over the sea.

441 Even though annual CO emissions in Western Europe may be well known, with uncertainties
442 of 6% according to Super et al., [2020], larger uncertainties could affect Eastern Europe.
443 Moreover, large uncertainties still affect bottom-up emission inventories at the 0.5°
444 resolution: spatial disaggregation of the national scale estimates to provide such gridded
445 estimates causes a significant increase in the uncertainty for CO [Super et al., 2020]. For the
446 inversion of CO emissions, the error standard deviations assigned to the prior CO emissions
447 at 7-day and 0.5° resolution are 100%. For this CO illustration, the covariance matrix B of the
448 prior errors is defined as diagonal (i.e. only variances in the individual control variables listed
449 in 4.2.1 are taken into account). With such a set-up, in theory, we could obtain negative
450 posterior emissions since the inversion system does not impose a constraint of positivity in the

451 **results. Nevertheless, even 100% of uncertainty lead to a prior distribution mostly (>80%) on**
452 **the positive side. The assimilation of data showing an increase above the background (at the**
453 **edges of the domain; not shown) further drive the inversion towards positive emissions for**
454 **both CO and NO_x inversions. In practice, our inversion does not lead to negative posterior**
455 **emissions (Figure 7b). Spatial and temporal correlations in B would further limit the**
456 **probability to get negative emissions locally by smoothing the posterior emissions at a spatial**
457 **scale at which the “aggregated” prior uncertainty is smaller than 100%. However, a positivity**
458 **constraint should be implemented in future versions of the system.**

459

460 **Based on the sensitivity test in Figure 5, the errors assigned to the CO lateral boundary**
461 **conditions and to their initial conditions are set at 15%. As these relative errors are**
462 **significantly lower than those for the emissions and as variations in the CO surface**
463 **concentrations are mainly driven by emissions (Figure 4), we assume a small relative influence**
464 **of the correction of initial and boundary conditions on our results.** The variance of the
465 individual observation errors in **R** is defined as the quadratic sum of the measurement error reported
466 in the MOPITT and the OMI data sets, and of the CTM errors (including **chemistry and** transport
467 errors and representativity errors) set at 20% of the retrieval values. The representativity errors
468 could have been reduced with the choice of a finer CTM resolution (e.g., with a resolution closer to
469 the size of the satellite pixel). Error correlations between the super-observations are neglected, so
470 that the covariance matrix **R** of the observation errors is diagonal.

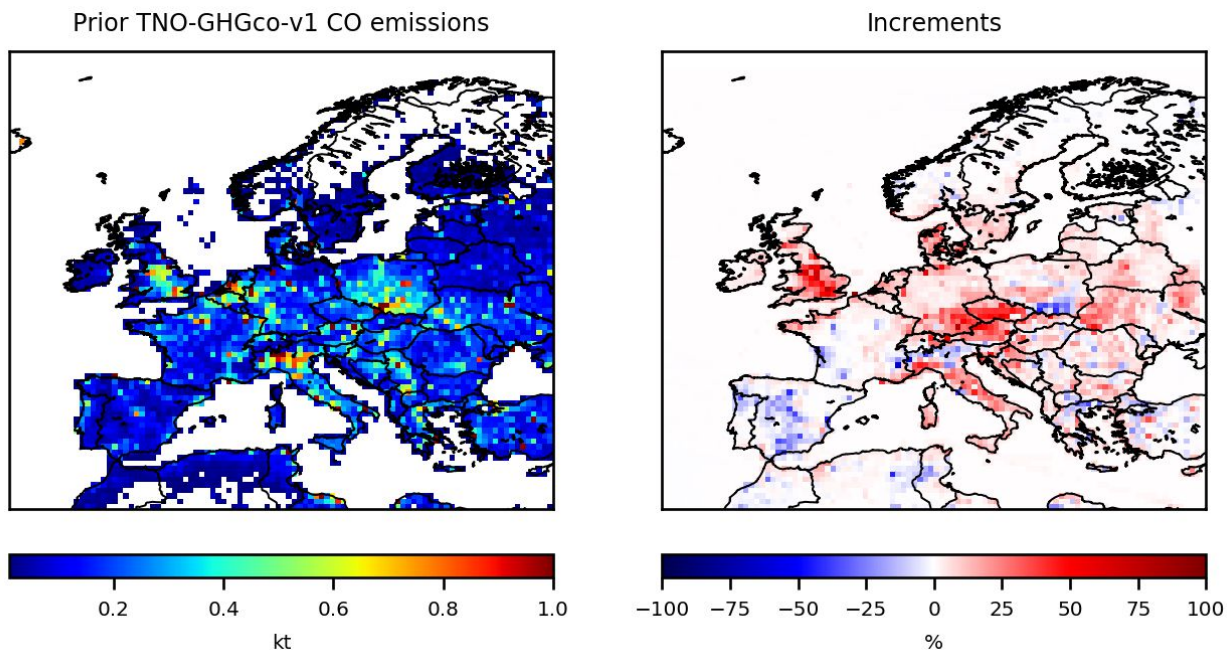
471

4.2.3 Inversion of CO emissions

472

473 **Ten iterations are needed to reduce the norm of the gradient of *J* by 90% with the**
474 **minimization algorithm M1QN3 and obtain the increments, i.e. the corrections provided by the**
475 **inversion. The prior CO emissions over Europe for the first week of March 2015 and their**
476 **increments are shown in Figure 7. As expected from the large differences between the prior**
477 **surface concentrations (Figure 6a) and the MOPITT observations (Figure 6b), local**
478 **increments can reach more than +50% (Figure 8b). CO emissions are increased over Central**
479 **and Eastern Europe, except in the south of Poland. On the contrary, CO emissions are**
480 **decreased over Spain and Portugal.** The analyzed concentrations are the concentrations simulated
481 by CHIMERE with the posterior fluxes: as expected, the optimization of the fluxes improves the fit
482 of the simulated concentrations to the observations (Figure 6c), particularly over Central and
483 Eastern Europe. **Over this area (see the grey box in Figure 6), the mean bias between the**

484 simulation and the observations has been reduced by about 27% when using the posterior
485 emissions (mean bias of 11.6 ppbv) instead of the prior emissions (mean bias of 15.9 ppbv).

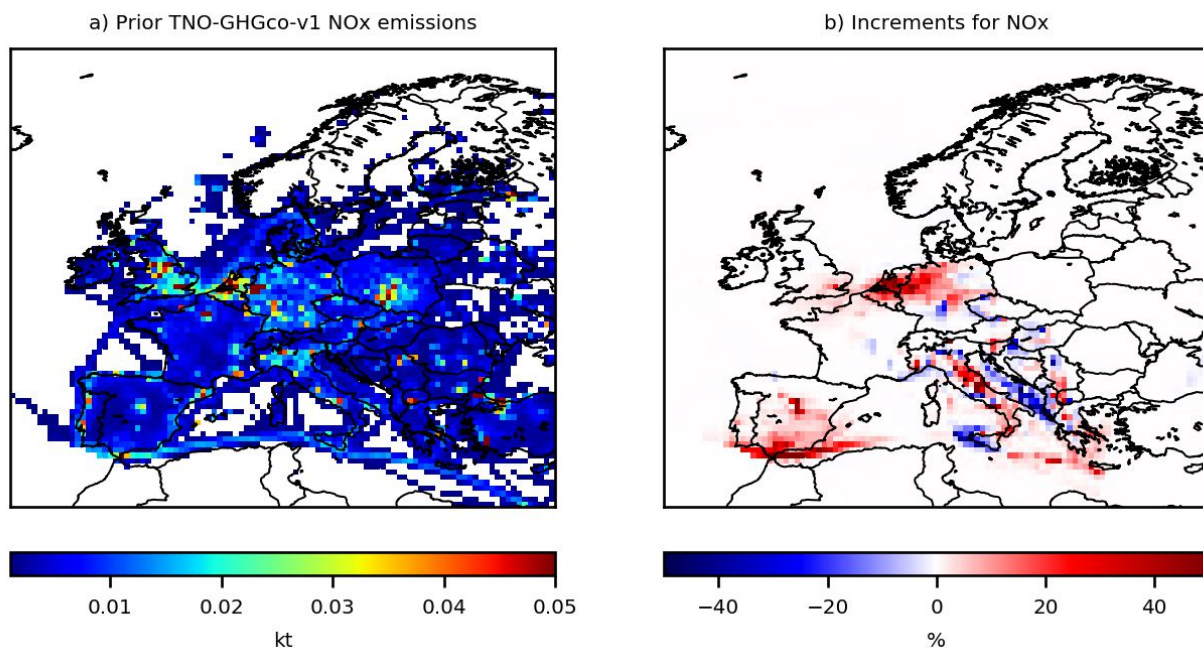


486 **Figure 8.** a) TNO-GHGco-v1 CO anthropogenic prior emissions, in ktCO/grid-cell and b)
487 increments provided by the inversion with constraints from MOPITTv8-NIR-TIR from the 1st to the
488 7th, March 2015, in %.

490

4.2.4. Inversion of NO_x emissions

491 The prior NO_x emissions are shown in Figure 9a. Three iterations are needed to reduce the
492 norm of the gradient of J by 90% with the minimization algorithm M1QN3 and obtain the
493 increments shown in Figure 9b. As expected from the underestimation of the prior tropospheric
494 columns in Figure 7, local increments may be large, for example over industrial areas (e.g., over the
495 Po Valley) and over the Netherlands, with increments of more than +30% (Figure 9b). The
496 analyzed NO₂ tropospheric columns in Figure 7c are the columns simulated by CHIMERE
497 with the NO₂ posterior fluxes: as expected, the optimization of the fluxes improves the fit of
498 the simulated concentrations to the observations, particularly over the Netherlands. Over this
499 area (see the grey box in Figure 7), the mean bias between the simulation and the observations
500 has been reduced by about 24% when using the posterior emissions (mean bias of $1.4e^{+15}$
501 molec.cm⁻²) instead of the prior emissions (mean bias of $1.8e^{+15}$ molec.cm⁻²). The posterior
502 emissions and their uncertainties will have to be evaluated and may bring hints to the cause of the
503 discrepancies.



504

505 **Figure 9.** a) TNO-GHGco-v1 NO_x anthropogenic prior emissions, in ktNO₂/grid-cell and b)
 506 increments provided by the inversion with constraints from OMI the 19th, February 2015, in %.

507 **5. Conclusion/Discussion**

508 This paper presents the Bayesian variational inverse system PYVAR-CHIMERE, which has been
 509 adapted to the inversion of reactive species such as CO and NO_x, taking advantage of the previous
 510 developments for long-lived species such as CO₂ [Broquet et al., 2011] and CH₄ [Pison et al.,
 511 2018]. We show the potential of PYVAR-CHIMERE, with inversions for CO and NO_x illustrated
 512 over Europe. PYVAR-CHIMERE will now be used to infer CO and NO_x emissions over long
 513 periods, e.g. first for a whole season or year and then for the recent decade 2005-2015 in the
 514 framework of the H2020 VERIFY project over Europe, and in the framework of the ANR
 515 PolEASIA over China, to quantify their trend and their spatio-temporal variability.

516

517 The PYVAR-CHIMERE system can handle any large number of both control parameters and
 518 observations. It will be able to cope with the dramatic increase in the number of data in the near
 519 future with, for example, the high-resolution imaging (pixel of 7x3.5 km²) of the new Sentinel-
 520 5P/TROPOMI program, launched in October 2017. These new space missions with high-resolution
 521 imaging have indeed the ambition to monitor atmospheric chemical composition for the
 522 quantification of anthropogenic emissions. Moreover, a step forward in the joint assimilation of co-
 523 emitted pollutants will soon be possible with the PYVAR-CHIMERE system and the availability of
 524 TROPOMI co-localized images of CO and NO₂. This should improve the consistency of the
 525 inversion results and can be used to inform inventory compilers, and subsequently improve

526 emission inventories. Moreover, this development will help in further understanding air quality
527 problems and addressing air quality related emissions at the national to subnational scales.

528

529 **Author Contribution**

530 All authors have contributed to the manuscript writing (main authors: AFC, GB, IP and GD) and to
531 the development of the present version of the PYVAR-CHIMERE system (main developer: IP). IP
532 and GD have parallelized the adjoint version from Menut et al., [2000], Menut et al., [2003] and
533 Pison et al., [2007]. IP has complemented the adjoint of new parameterizations since the CHIMERE
534 release in 2011 and the tangent-linear model.

535

536 **Code and Data Availability**

537 OMI QA4ECV NO₂ product can be found here: <http://temis.nl/qa4ecv/no2.html>.

538 MOPITTv8-NIR-TIR CO product can be found here: <ftp://15ftl01.larc.nasa.gov/MOPITT/>

539 The CHIMERE code is available here: www.lmd.polytechnique.fr/chimere/.

540

541 The associated documentation of PYVAR-CHIMERE is available on the website
542 <https://pyvar.lsce.ipsl.fr/doku.php/3chimere:headpage>. The documentation includes a whole
543 description of PYVAR-CHIMERE and several tutorials on how to run a first PYVAR-CHIMERE
544 simulation or how to run an inversion.

545

546 **Competing interests**

547 The authors declare that they have no conflict of interest.

548

549 **Acknowledgements**

550 We acknowledge L. Menut and C. Schmechtig for their contributions to the development work on
551 the adjoint code of CHIMERE and its parallelization. We acknowledge the TNO team (H.A. Denier
552 van der Gon, J. Kuenen, S. Dellaert, S. Jonkers, A. Visschedijk, et al.) for providing NO_x and CO
553 emissions over Europe. We also acknowledge the free use of tropospheric NO₂ column data from
554 the OMI sensor from <http://temis.nl/qa4ecv/no2.html> and the free use of CO surface concentrations
555 from the MOPITT sensor from <ftp://15ftl01.larc.nasa.gov/MOPITT/>. For this study, A. Fortems-
556 Cheiney was funded by the French Space Agency-Centre National d'Etudes Spatiales CNES and by
557 the H2020 VERIFY project, funded by the European Commission Horizon 2020 research and
558 innovation programme, under agreement number 776810. L. Costantino was funded by the
559 PolEASIA ANR project under the allocation ANR-15-CE04-0005. This work was granted access to
560 the HPC resources of TGCC under the allocation A0050107232 made by GENCI. Finally, we wish
561 to thank F. Marabelle (LSCE) and his team for computer support.

562

563 **References**

564

565

566

567 Belikov, D. A., Maksyutov, S., Yaremchuk, A., Ganshin, A., Kaminski, T., Blessing, S.,
568 Sasakawa, M., Gomez-Pelaez, A. J., and Starchenko, A.: Adjoint of the global Eulerian–Lagrangian
569 coupled atmospheric transport model (A-GELCA v1.0): development and validation, *Geosci.*
570 *Model Dev.*, 9, 749–764, <https://doi.org/10.5194/gmd-9-749-2016>, 2016.

571

572 Boersma, K. F., Vinken, G. C. M., and Eskes, H. J.: Representativeness errors in comparing
573 chemistry transport and chemistry climate models with satellite UV–Vis tropospheric column
574 retrievals, *Geosci. Model Dev.*, 9, 875–898, <https://doi.org/10.5194/gmd-9-875-2016>, 2016.
575

576 Boersma, K. F., Eskes, H., Richter, A., De Smedt, I., Lorente, A., Beirle, S., Van Geffen, J.,
577 Peters, E., Van Roozendaal, M. and Wagner, T.: QA4ECV NO₂ tropospheric and stratospheric
578 vertical column data from OMI (Version 1.1) [Data set], Royal Netherlands Meteorological Institute
579 (KNMI), <http://doi.org/10.21944/qa4ecv-no2-omi-v1.1>, 2017.
580

581 Bousquet, P., P. Ciais, P. Peylin, M. Ramonet, and P. Monfray: Inverse modeling of annual
582 atmospheric CO₂ sources and sinks: 1. Method and control inversion, *J. Geophys. Res.*, 104(D21),
583 26,161 – 26,178, doi:10.1029/1999JD900342, 1999.
584

585 Broquet, G., Chevallier, F., Rayner, P., Aulagnier, C., Pison, I., Ramonet, M., Schmidt, M.,
586 Vermeulen, A. T., and Ciais, P.: A European summertime CO₂ biogenic flux inversion at mesoscale
587 from continuous in situ mixing ratio measurements, *J. Geophys. Res.*, 116, D23303, doi:
588 10.1029/2011JD016202, 2011.
589

590 Broquet, G., Chevallier, F., Bréon, F.-M., Kadygrov, N., Alemanno, M., Apadula, F.,
591 Hammer, S., Haszpra, L., Meinhardt, F., Morguá, J. A., Necki, J., Piacentino, S., Ramonet, M.,
592 Schmidt, M., Thompson, R. L., Vermeulen, A. T., Yver, C., and Ciais, P.: Regional inversion of
593 CO₂ ecosystem fluxes from atmospheric measurements: reliability of the uncertainty estimates,
594 *Atmos. Chem. Phys.*, 13, 9039–9056, <https://doi.org/10.5194/acp-13-9039-2013>, 2013.
595

596 Chevallier, F., M. Fisher, P. Peylin, S. Serrar, P. Bousquet, F.-M. Bréon, A. Chédin, and P.
597 Ciais: Inferring CO₂ sources and sinks from satellite observations: method and application to TOVS
598 data, *J. Geophys. Res.*, 110, D24309, <doi:10.1029/2005JD006390>, 2005.
599

600 Chevallier, F., Ciais, P., Conway, T. J., Aalto, T., Anderson, B. E., Bousquet, P., Brunke, E.
601 G., Ciattaglia, L., Esaki, Y., Fröhlich, M., Gomez, A., Gomez-Pelaez, A. J., Haszpra, L., Krummel,
602 P. B., Langenfelds, R. L., Leuenberger, M., Machida, T., Maignan, F., Matsueda, H., Morguá, J. A.,
603 Mukai, H., Nakazawa, T., Peylin, P., Ramonet, M., Rivier, L., Sawa, Y., Schmidt, M., Steele, L. P.,
604 Vay, S. A., Vermeulen, A. T., Wofsy, S., and Worthy, D.: CO₂ surface fluxes at grid point scale
605 estimated from a global 21 year reanalysis of atmospheric measurements, *J. Geophys. Res.*, 115, 1–
606 17, <https://doi.org/10.1029/2010jd013887>, 2010.
607

608 CHIMERE documentation,
609 <https://www.lmd.polytechnique.fr/chimere/docs/CHIMEREdoc2017.pdf>, Last update of this
610 documentation: June 8, 2017,2017.
611

612 Deeter, M. N., Edwards, D. P., Francis, G. L., Gille, J. C., Mao, D., Martinez-Alonso, S.,
613 Worden, H. M., Ziskin, D., and Andreae, M. O.: Radiance-based Retrieval Bias Mitigation for the
614 MOPITT Instrument: The Version 8 Product, *Atmos. Meas. Tech. Discuss.*,
615 <https://doi.org/10.5194/amt-2019-41>, in review, 2019.
616

617 Ding, J., Miyazaki, K., van der A, R. J., Mijling, B., Kurokawa, J.-I., Cho, S., Janssens-
618 Maenhout, G., Zhang, Q., Liu, F., and Levelt, P. F.: Intercomparison of NO_x emission inventories
619 over East Asia, *Atmos. Chem. Phys.*, 17, 10125–10141, <https://doi.org/10.5194/acp-17-10125-2017>,
620 2017.
621

622 EEA, Air quality in Europe - 2018 report, 12/2018,
623 <https://www.eea.europa.eu/publications/air-quality-in-europe-2018>.

624
625
626
627
628
629
630
631
632
633
634
635
636
637
638
639
640
641
642
643
644
645
646
647
648
649
650
651
652
653
654
655
656
657
658
659
660
661
662
663
664
665
666
667
668
669
670
671
672

Elbern, H., Strunk, A., Schmidt, H., and Talagrand, O.: Emission rate and chemical state estimation by 4-dimensional variational inversion, *Atmos. Chem. Phys.*, 7, 3749-3769, <https://doi.org/10.5194/acp-7-3749-2007>, 2007.

EMEP/EEA air pollutant emission inventory guidebook, 2016.

EMEP/CEIP,

https://ceip.at/ms/ceip_home1/ceip_home/webdab_emepdatabase/emissions_emepmodels/

de Foy, B., Lu, Z. and Streets, D.G.: Satellite NO₂ retrievals suggest China has exceeded its NO_x reduction goals from the twelfth Five-Year Plan, *Nature Scientific Reports*, 6:35912, 2016.

Fisher, M., and P. Courtier: Estimating the covariance matrices of analysis and forecast error in variational data assimilation, Tech. Mem. 220, 26 pp., Eur. Cent. for Medium-Range Weather Forecasting, Reading, U. K., 1995.

Gilbert, J., and C. Lemaréchal (1989), Some numerical experiments with variable storage quasi Newton algorithms, *Math. Program.*, 45, 407–435.

Hein, R., et coll.: An inverse modeling approach to investigate the global atmospheric methane cycle, *Global. Biogeochem. Cycles*, 11, 43-76, 1997.

Henze, D. K., Hakami, A., and Seinfeld, J. H.: Development of the adjoint of GEOS-Chem, *Atmos. Chem. Phys.*, 7, 2413–2433, <https://doi.org/10.5194/acp-7-2413-2007>, 2007.

Hooghiemstra, P. B., Krol, M. C., Bergamaschi, P., de Laat, A. T. J., van der Werf, G. R., Novelli, P.C., Deeter, M. N., Aben, I., and Rockmann, T.: Comparing optimized CO emission estimates using MOPITT or NOAA surface network observations, *J. Geophys. Res.*, 117, D06309, doi:10.1029/2011JD017043, 2012.

Kadyrov, N., Broquet, G., Chevallier, F., Rivier, L., Gerbig, C., and Ciais, P.: On the potential of the ICOS atmospheric CO₂ measurement network for estimating the biogenic CO₂ budget of Europe, *Atmos. Chem. Phys.*, 15, 12765–12787, <https://doi.org/10.5194/acp-15-12765-2015>, 2015.

Konovalov, I. B. et coll.: Inverse modelling of the spatial distribution of NO emissions on a continental scale using satellite data, *Atmos. Chem. Phys.*, 6, 1747-1770, doi:10.5194/acp-6-1747-2006, 2006.

Konovalov, I. B., Beekmann, M., Burrows, J. P., and Richter, A.: Satellite measurement based estimates of decadal changes in European nitrogen oxides emissions, *Atmos. Chem. Phys.*, 8, 2623-2641, doi:10.5194/acp-8-2623-2008, 2008.

Konovalov, I. B., Beekmann, M., Richter, A., Burrows, J. P., and Hilboll, A.: Multi-annual changes of NO_x emissions in megacity regions: nonlinear trend analysis of satellite measurement based estimates, *Atmos. Chem. Phys.*, 10, 8481-8498, doi:10.5194/acp-10-8481-2010, 2010.

673 Koohkan, M. R., Bocquet, M., Roustan, Y., Kim, Y., and Seigneur, C.: Estimation of
674 volatile organic compound emissions for Europe using data assimilation, *Atmos. Chem. Phys.*, 13,
675 5887-5905, <https://doi.org/10.5194/acp-13-5887-2013>, 2013.

676

677 Kuenen, J. J. P., Visschedijk, A. J. H., Jozwicka, M., and Denier van der Gon, H. A. C.:
678 TNO-MACC_II emission inventory; a multi-year (2003–2009) consistent high-resolution European
679 emission inventory for air quality modelling, *Atmos. Chem. Phys.*, 14, 10963-10976,
680 <https://doi.org/10.5194/acp-14-10963-2014>, 2014.

681

682 Kurokawa, J., Ohara, T., Morikawa, T., Hanayama, S., Janssens-Maenhout, G., Fukui, T.,
683 Kawashima, K., and Akimoto, H.: Emissions of air pollutants and greenhouse gases over Asian
684 regions during 2000–2008: Regional Emission inventory in ASia (REAS) version 2, *Atmos. Chem.*
685 *Phys.*, 13, 11019-11058, doi:10.5194/acp-13-11019-2013, 2013.

686

687 Lattuati, M., Impact des émissions européennes sur le bilan de l'ozone troposphérique a
688 l'interface de l'europe et de l'atlantique nord : apport de la modélisation lagrangienne et des mesures
689 en altitude, Ph.D. thesis, Université Paris VI, 1997.

690

691 Lelieveld, J., Klingmüller, K., Pozzer, A., Pöschl, U., Fnais, M., Daiber, A., Münzel, T.;
692 Cardiovascular disease burden from ambient air pollution in Europe reassessed using novel hazard
693 ratio functions, *European Heart Journal*, , ehz135, <https://doi.org/10.1093/eurheartj/ehz135>, 2019.

693

694 Lin, J.-T., McElroy, M. B., and Boersma, K. F.: Constraint of anthropogenic NO_x emissions
695 in China from different sectors: a new methodology using multiple satellite retrievals, *Atmos. Chem.*
696 *Phys.*, 10, 63-78, doi:10.5194/acp-10-63-2010, 2010.

697

698 Liu, F., Beirle, S., Zhang, Q., Dörner, S., He, K., and Wagner, T.: NO_x lifetimes and
699 emissions of cities and power plants in polluted background estimated by satellite observations,
700 *Atmos. Chem. Phys.*, 16, 5283–5298, <https://doi.org/10.5194/acp-16-5283-2016>, 2016.

701

702 Locatelli, R., Bousquet, P., Saunois, M., Chevallier, F., and Cressot, C.: Sensitivity of the
703 recent methane budget to LMDz sub-grid-scale physical parameterizations, *Atmos. Chem. Phys.*,
704 15, 9765-9780, <https://doi.org/10.5194/acp-15-9765-2015>, 2015.

705

706 Mailler S., L. Menut, D. Khvorostyanov, M. Valari, F. Couvidat, G. Siour, S. Turquety, R.
707 Briant, P. Tuccella, B. Bessagnet, A. Colette, L. Letinois, and F. Meleux, CHIMERE-2017: from
708 urban to hemispheric chemistry-transport modeling ,*Geosci. Model Dev.*, 10, 2397-2423,
709 <https://doi.org/10.5194/gmd-10-2397-2017>, 2017.

710

711 Menut, L., R. Vautard, M. Beekmann, and C. Honoré: Sensitivity of photochemical
712 pollution using the adjoint of a simplified chemistry-transport model, *J. Geophys. Res.*, 105,
713 15,379–15,402, 2000.

714

715 Menut L.: Adjoint modelling for atmospheric pollution processes sensitivity at regional
716 scale during the ESQUIF IOP2, *Journal of Geophysical Research - Atmospheres*, 108, D17,
717 <https://doi.org/10.1029/2002JD002549>, 2003.

718

719 Menut, L., Goussebaile, A., Bessagnet, B., Khvorostiyarov, D., and Ung, A.: Impact of
720 realistic hourly emissions profiles on air pollutants concentrations modelled with CHIMERE,
721 *Atmospheric Environment*, 49, 233–244, doi:10.1016/j.atmosenv.2011.11.057, 2012.

722 Menut, L., Bessagnet, B., Khvorostyanov, D., Beekmann, M., Blond, N., Colette, A., Coll,
723 I., Curci, G., Foret, G., Hodzic, A., Mailler, S., Meleux, F., Monge, J.-L., Pison, I., Siour,
724 G.,Turquety, S., Valari, M., Vautard, R., and Vivanco, M. G.: CHIMERE 2013: a model for
725 regional atmospheric composition modelling, *Geosci. Model Dev.*, 6, 981–1028, doi:10.5194/gmd-
726 6-981-2013, 2013.

727

728 Mijling, B., and R. J. van der A: Using daily satellite observations to estimate emissions of
729 short-lived air pollutants on a mesoscopic scale, *J. Geophys. Res.*, 117, D17302,
730 doi:10.1029/2012JD017817, 2012.

731

732 Mijling, B., et al., Regional nitrogen oxides emission trends in East Asia observed from
733 space, *Atmos. Chem. Phys.*, 3, 12003, 2013.

734

735 Muller, J.-P., Kharbouche, S., Gobron, N., Scanlon, T., Govaerts, Y., Danne, O., Schultz, J.,
736 Lattanzio, A., Peters, E., De Smedt, I., Beirle, S., Lorente, A., Coheur, P. F., George, M., Wagner,
737 T., Hilboll, A., Richter, A., Van Roozendaal, M., and Boersma, K. F.: Recommendations
738 (scientific) on best practices for retrievals for Land and Atmosphere ECVs (QA4ECV Deliverable
739 4.2 version 1.0), 186 pp., available at: <http://www.qa4ecv.eu/sites/default/files/D4.2.pdf> (last
740 access: 12 April 2018), 2016.

741

742 Owens, R. G. and Hewson, T.: ECMWF Forecast User Guide, Reading,
743 <https://doi.org/10.21957/m1cs7h>,[https://software.ecmwf.int/wiki/display/FUG/Forecast+User+Guid](https://software.ecmwf.int/wiki/display/FUG/Forecast+User+Guide)
744 [e](https://software.ecmwf.int/wiki/display/FUG/Forecast+User+Guide), 2018.

745

746 Pison, I., Menut, L., and Bergametti, G.: Inverse modeling of surface NO_x anthropogenic
747 emission fluxes in the Paris area during the ESQUIF campaign, *J. Geophys. Res. Atmos.*, 112,
748 D24302, doi:10.1029/2007JD008871, 2007.

749

750 Pison, I., Bousquet, P., Chevallier, F., Szopa, S., and Hauglustaine, D.: Multi-species
751 inversion of CH₄, CO and H₂ emissions from surface measurements, *Atmospheric Chemistry and*
752 *Physics*, 9, 5281-5297, 2009.

753

754 Pison, I., A. Berchet, M. Saunois, .How a European network may constrain methane
755 emissions at the French national scale. *Atmospheric Chemistry and Physics*, 2018.

756

757 Stavrakou, T. and J.-F. Müller: Grid-based versus big region approach for inverting CO
758 emissions using Measurement of Pollution in the Troposphere (MOPITT) data, *Journal of*
759 *Geophysical Research: Atmospheres*, 111, D15, 2006.

760

761 Stavrakou, T., Muller, J.-F., Boersma, K. F., De Smedt, I., and van der A, R. J.: Assessing
762 the distribution and growth rates of NO_x emission sources by inverting a 10-year record of NO₂
763 satellite columns, *Geophys. Res. Lett.*, 35, 1–5, doi:10.1029/2008GL033521, 2008.

764

765 Super, I., Dellaert, S. N. C., Visschedijk, A. J. H., and Denier van der Gon, H. A. C.:
766 Uncertainty analysis of a European high-resolution emission inventory of CO₂ and CO to support
767 inverse modelling and network design, *Atmos. Chem. Phys.*, 20, 1795–1816,
768 <https://doi.org/10.5194/acp-20-1795-2020>, 2020.

769

770 Szopa, S., Foret, G., Menut, L., and Cozic, A.: Impact of large scale circulation on European
771 summer surface ozone: consequences for modeling, *Atmospheric Environment*, 43, 1189–
772 1195, doi:10.1016/j.atmosenv.2008.10.039, 2008.

773

774 Talagrand, O. : Assimilation of observations : an introduction, *J. Met. Soc., Japan*, 75, 191-
775 209, 1997.
776
777 Valin, L. C., Russell, A. R., and Cohen, R. C.: Variations of OH radical in an urban
778 plume inferred from NO₂ column measurements, *Geophys. Res. Lett.*, 40, 1856–1860,
779 doi:10.1002/grl.50267, 2013.
780
781 van der A, R. J., Mijling, B., Ding, J., Koukouli, M. E., Liu, F., Li, Q., Mao, H., and Theys,
782 N.: Cleaning up the air: Effectiveness of air quality policy for SO₂ and NO_x emissions in China,
783 *Atmos. Chem. Phys.*, 17, 1775-1789, 2017.
784
785 Vestreng, V., Breivik, K., Adams, M., Wagner, A., Goodwin, J., Rozovskaya, O.,
786 and Oacyna, J. . Inventory Review 2005 - Emission Data reported to CLRTAP and under the NEC
787 Directive - Initial review for HMs and POPs .EMEP Status report, Norwegian Meteorological
788 Institute, Oslo, 2005.
789
790
791 Yin, Y., Chevallier, F., Ciais, P., Broquet, G., A. Fortems-Cheiney, Pison, I. and Saunois,
792 M: Decadal trends in global CO emissions as seen by MOPITT, *Atmos. Chem. Phys.*, 15, 13433-
793 13451, 2015.
794
795 Yumimoto, K. and Uno, I.: Adjoint inverse modeling of CO emissions over Eastern Asia
796 using four-dimensional variational data assimilation, *Atmospheric Environment*, 40, 35, 6836-6845,
797 DOI: 10.1016/j.atmosenv.2006.05.042, 2006.
798
799 Wang, Y., G. Broquet, P. Ciais, F. Chevallier, F. Vogel, N. Kadyrov, L. Wu, Y. Yin, R.
800 Wang and S. Tao: Estimation of observation errors for large-scale atmospheric inversion of
801 CO₂ emissions from fossil fuel combustion, *Tellus B: Chemical and Physical Meteorology*, 69:1,
802 DOI: [10.1080/16000889.2017.1325723](https://doi.org/10.1080/16000889.2017.1325723), 2017.
803
804 Wang, Y., Broquet, G., Ciais, P., Chevallier, F., Vogel, F., Wu, L., Yin, Y., Wang, R., and
805 Tao, S.: Potential of European ¹⁴CO₂ observation network to estimate the fossil fuel CO₂ emissions
806 via atmospheric inversions, *Atmos. Chem. Phys.*, 18, 4229–4250, [https://doi.org/10.5194/acp-18-](https://doi.org/10.5194/acp-18-4229-2018)
807 4229-2018, 2018.
808
809 WHO World Health Organization: Ambient Air Pollution: a global assessment of exposure
810 and burden of disease, 2016.
811
812 Zheng, T., French, N. H. F., and Baxter, M.: Development of the WRF-CO₂ 4D-Var
813 assimilation system v1.0, *Geosci. Model Dev.*, 11, 1725–1752, [https://doi.org/10.5194/gmd-11-](https://doi.org/10.5194/gmd-11-1725-2018)
814 1725-2018, 2018.
815
816 Zheng, B., Chevallier, F., Yin, Y., Ciais, P., Fortems-Cheiney, A., Deeter, M. N., Parker, R.
817 J., Wang, Y., Worden, H. M., and Zhao, Y.: Global atmospheric carbon monoxide budget 2000–
818 2017 inferred from multi-species atmospheric inversions, *Earth Syst. Sci. Data*, 11, 1411–1436,
819 <https://doi.org/10.5194/essd-11-1411-2019>, 2019.